Check for updates

Advanced Materials

ADVANCED MATERIALS
www.advmat.de

RESEARCH ARTICLE OPEN ACCESS

Above Room Temperature Ferroelectricity in Epitaxially Strained $KTaO_3$

Tobias Schwaigert[1,2] | Salva Salmani-Rezaie[3,4,5] | Sankalpa Hazra[6] | Utkarsh Saha[6] | Maya Ramesh[2] | Aiden Ross[6] | Betül Pamuk[7] | Long-Qing Chen[6] | David A. Muller[3,4] | Darrell G. Schlom[1,2,4,8] | Venkatraman Gopalan[6,9] | Kaveh Ahadi[5,10]

[1]Platform for the Accelerated Realization, Analysis, and Discovery of Interface Materials (PARADIM), Cornell University, Ithaca, New York, USA | [2]Department of Materials Science and Engineering, Cornell University, Ithaca, New York, USA | [3]School of Applied and Engineering Physics, Cornell University, Ithaca, New York, USA | [4]Kavli Institute at Cornell for Nanoscale Science, Cornell University, Ithaca, New York, USA | [5]Department of Materials Science and Engineering, Ohio State University, Columbus, Ohio, USA | [6]Department of Materials Science and Engineering, Pennsylvania State University, University Park, Pennsylvania, USA | [7]Department of Physics and Astronomy, Williams College, Williamstown, Massachusetts, USA | [8]Leibniz-Institut für Kristallzüchtung, Berlin, Germany | [9]Department of Physics, Pennsylvania State University, University Park, Pennsylvania, USA | [10]Department of Electrical and Computer Engineering, Ohio State University, Columbus, Ohio, USA

Correspondence: Kaveh Ahadi (ahadi.4@osu.edu)

Received: 21 January 2026 | **Revised:** 19 June 2026 | **Accepted:** 17 July 2026

Keywords: condensed matter physics | curie temperature | epitaxy | ferroelectricity | heterojunction | materials science | polarization density | thin film

ABSTRACT

Epitaxial strain is a powerful means to engineer emergent phenomena in thin films and heterostructures. Here, we demonstrate that $KTaO_3$, a cubic perovskite in bulk form, can be epitaxially strained into a highly tunable ferroelectric. $KTaO_3$ films grown commensurate to $SrTiO_3$ (001) substrates experience an in-plane strain of −2.1 % that transforms the cubic structure into a tetragonal polar phase with a transition temperature of 475 K, consistent with our thermodynamic calculations. We show that the Curie temperature and the spontaneous electric polarization can be systematically controlled with epitaxial strain. Scanning transmission electron microscopy reveals cooperative polar displacements of the potassium columns with respect to the neighboring tantalum columns at room temperature. Optical second-harmonic generation results are described by a tetragonal polar point group (4*mm*), indicating the emergence of a global polar ground state. We observe a ferroelectric hysteresis response using metal–insulator–metal capacitor test structures. The results demonstrate a robust intrinsic ferroelectric state in epitaxially strained $KTaO_3$ thin films.

1 | Introduction

The ability to precisely tune specific properties defines the success of any materials system as a platform for new technologies. The misfit to an underlying substrate can impart an enormous strain to films and heterostructures, exceeding the failure limit of bulk samples and modifying their energy landscape. Consequently, epitaxial strain can be harnessed as a tuning knob for emergent phenomena and functional properties. For example, epitaxial strain enhancement of transistor mobility [1] or the transition temperature in ferromagnets [2, 3], ferroelectrics [4], and superconductors [5] have been achieved. Even more exciting is when the epitaxial strain reveals a hidden ground state, such as ferromagnetism [6], ferroelectricity [6, 7], and

Tobias Schwaigert, Salva Salmani-Rezaie, and Sankalpa Hazra contributed equally to this work.

This is an open access article under the terms of the Creative Commons Attribution License, which permits use, distribution and reproduction in any medium, provided the original work is properly cited.
© 2026 The Author(s). *Advanced Materials* published by Wiley-VCH GmbH

superconductivity [8] that are absent in the unstrained bulk form of that material system.

Thin films of ferroelectric materials play an essential role in high-density memory devices [9], which makes the ability to control their ferroelectricity of great interest. For practical device applications and fundamental studies, it is equally desirable to tune the ferroelectric transition over a wide temperature range, from above room temperature to cryogenic temperatures, enabling operation in diverse environments and revealing temperature-dependent phenomena. Strong coupling between strain and ferroelectricity makes epitaxial strain a particularly efficient tuning knob to control electric polarization and ferroelectricity [10, 11].

The efficiency of strain control of ferroelectricity is captured by the strain derivatives of key properties, such as $dT_c/d\varepsilon\%$ and $dP_r/d\varepsilon\%$, which quantify the change in transition temperature and remanent polarization per unit strain. For example, while the bulk $SrTiO_3$ is paraelectric, epitaxially strained $SrTiO_3$ films exhibit emergent ferroelectricity with Curie temperatures reaching room temperature [7, 12]. $dT_c/d\varepsilon$ and $dP_r/d\varepsilon$ are 83 K and 9 $\mu C\,cm^{-2}$, respectively, for $SrTiO_3$ [13]. $KTaO_3$ is a quantum paraelectric, that is close to a polar instability but remains paraelectric down to low temperature. With $dT_c/d\varepsilon = 361$ K and $dP_r/d\varepsilon = 9\,\mu C\,cm^{-2}$, $KTaO_3$ is an ideal candidate for epitaxial strain tuning of ferroelectricity despite its cubic ground state [14, 15].

Tunable electric polarization coupled with enhanced spin–orbit coupling, compared to $SrTiO_3$ [16], make $KTaO_3$ an intriguing candidate for spintronics applications [17]. The discovery of a 2D electron gas (2DEG) [18–20] and unconventional superconducting states [21–23] at $KTaO_3$ interfaces combined with reports of efficient spin-to-charge interconversion [24, 25] mark $KTaO_3$ as an ideal model system to explore these phenomena in the presence of switchable spontaneous polarization. For example, theoretical investigations suggest that Rashba spin splitting can be efficiently improved with the application of compressive stress [26]. Finally, recent theoretical and experimental results point to ferroelectric control and enhancement of superconductivity in incipient ferroelectrics [27–29].

$KTaO_3$ is primarily studied in bulk due to the lack of high-quality epitaxial thin films, which are critical for tuning its physical properties and any potential device applications. High-quality films grown under adsoprtion-controlled conditions by molecular-beam epitaxy (MBE) [30] and hybrid pulsed-laser depostion [31] have recently become available, enabling epitaxial strain engineering of $KTaO_3$ and experimental testing of theoretical predictions [32, 33]. Here, we demonstrate the epitaxial stabilization of the ferroelectric tetragonal polymorph of $KTaO_3$ by imposing epitaxial strain through commensurate epitaxial growth on various lattice mismatched substrates under in-plane compressive strain. The emergence of ferroelectricity is supported by DFT and thermodynamic calculations, the atomic-scale characterization of the polar displacements using HAADF-STEM, second-harmonic generation (SHG) rotational anisotropy response suggesting a $4mm$ point group, and the observation of ferroelectric hysteresis in metalinsulator–metal (MIM) heterostructures.

2 | Results

2.1 | Theoretical Considerations on the Formation of a Polar Point Group

$KTaO_3$ is a cubic perovskite with a lattice constant of $a_{KTO} = 3.988$ Å [34] at room temperature. The theoretical lattice parameter of cubic perovskite $KTaO_3$ with $Pm\bar{3}m$ (#221) symmetry is 3.990 Å, resolved from first-principles calculations. As the structure is compressively strained to simulate the properties when grown on $GdScO_3$ (−0.5%), $DyScO_3$ (−0.9%), and $SrTiO_3$ (−2.1%), the out-of-plane lattice parameter is relaxed for each tetragonal structure with the $P4/mmm$ (space group #123) symmetry. The ferroelectric transition temperature can be calculated by solving the equation $T_c = \max(T_C^1, T_C^2)$ where T_C^1 and T_C^2 are solutions to [35]

$$\alpha_1\left(T_C^1\right) + \Delta\alpha_1 = \alpha_1 T_C^1 - \frac{(Q_{11}+Q_{12})\epsilon_s}{s_{11}+s_{12}} = 0 \tag{1}$$

and

$$\alpha_1\left(T_C^2\right) + \Delta\alpha_3 = \alpha_1 T_C^2 - \frac{2Q_{12}\epsilon_s}{s_{11}+s_{12}} = 0 \tag{2}$$

where α_1 represents the first-order Landau coefficient, $\Delta\alpha_1$ and $\Delta\alpha_3$ denote the changes to the α_1 coefficient due to strain along the in-plane and out-of-plane directions, respectively, Q_{11} and Q_{12} are components of the electrostrictive tensor and s_{11}, s_{12} are the components of the elastic compliance tensor, ϵ_s is the misfit strain, and T_C^1 and T_C^2 are the transition temperatures due to the compressive and tensile strain, respectively. This allows us to construct the phase transition boundaries between the paraelectric and ferroelectric phases in the temperature–strain phase diagram marked by the dotted lines as illustrated in Figure 1. The dotted boundaries are calculated using a single set of coefficients (Tables S2 and S3). An extended derivation can be found in the Supporting Information II.

The paraelectric ($4/mmm$) phase in the figure has zero net polarization, that is, $P_1 = P_2 = P_3 = 0$. The ferroelectric phases are the tetragonal ($4mm$) phase with $P_1 = P_2 = 0, P_3 \neq 0$ and out-of-plane polarization, induced by a compressive in-plane stress, and the orthorhombic ($mm2$) phase $P_1 = P_2 = 0, P_3 \neq 0$ showing in-plane polarization due to the tensile in-plane stress.

Phonon calculations of the tetragonal structures with the $P4/mmm$ symmetry reveal a Γ-point instability with the A_{2u} symmetry and $\Gamma_3^-(a)$ irreducible representation, with eigenfrequency of $0.94i$, $2.57i$, and $4.22i$ THz, for each compressive strain, respectively. When the displacements of the atoms along this phonon frequency with $\omega = 4.22i$ are frozen into the tetragonal atomic structure, the symmetry is reduced to $P4mm$ (#99). This space group is energetically favored by 14 meV per formula unit compared to the parent $P4/mmm$ structure, for growth on $SrTiO_3$ with −2.1% compressive strain. The out-of-plane phonon frequency shows a significant hardening from the A_{2u} mode of the $P4/mmm$ structure to the A_1 mode of the $P4mm$ structure, indicating a second-order phase transition to the ferroelectric $P4mm$ structure upon compressive strain. The in-plane phonon frequency with the E symmetry is not significantly affected with increasing compressive strain. Upon application of tensile strain, $P4/mmm$ symmetry structure has a Γ-point instability with the

15214095, 2026, 57, Downloaded from https://advanced.onlinelibrary.wiley.com/doi/10.1002/adma.74366, Wiley Online Library on [16/11/2026]. See the Terms and Conditions (https://onlinelibrary.wiley.com/terms-and-conditions) on Wiley Online Library for rules of use; OA articles are governed by the applicable Creative Commons License

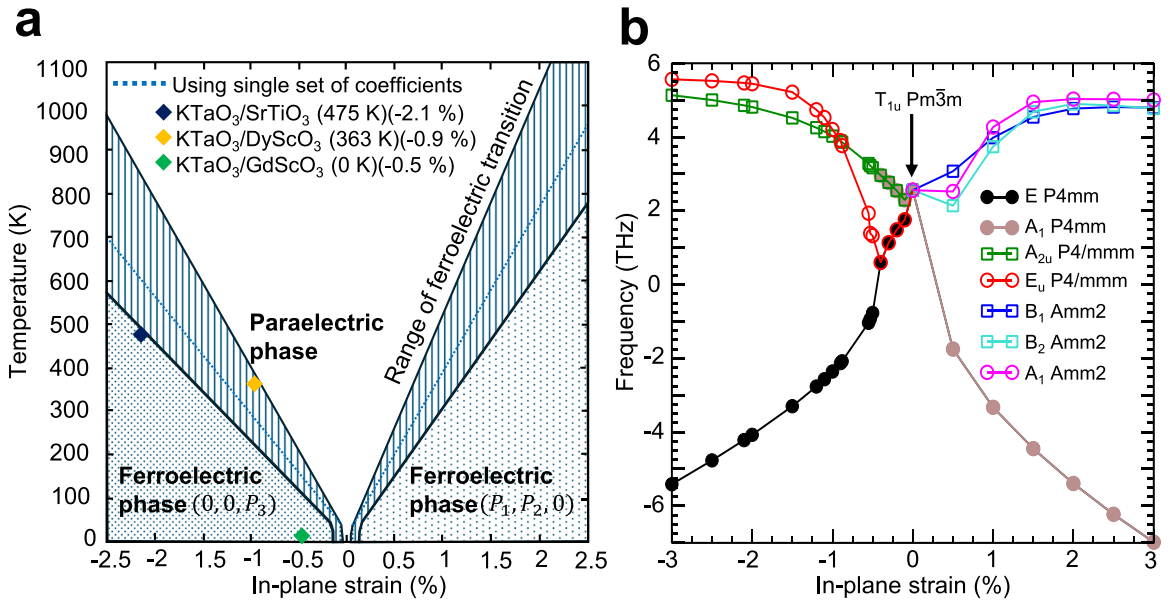


FIGURE 1 | Thermodynamic and DFT investigation of the epitaxial strain control of ferroelectricity in $KTaO_3$. (a) Expected shift in T_c of (001) $KTaO_3$, under epitaxial strain. The experimental values of T_c are from SHG experiments (Figure 4 and Figure S13). The components of the spontaneous polarization are given with respect to the pseudocubic axes of $KTaO_3$. (b) Lowest phonon frequencies of the structures with the $P4/mmm$, $P4mm$, and $Amm2$ symmetries as a function of epitaxial strain, with imaginary phonon frequencies presented as negative. Tetragonal structure with the $P4/mmm$ symmetry starts to have imaginary phonon frequency beyond 0.5% compressive (tensile) strain with the A_{2u} (E_u) symmetry. Freezing in this phonon mode leads to a ferroelectric phase transition to a structure with the $P4mm$ ($Amm2$) symmetry.

E_u symmetry and $\Gamma_5^-(a,-a)$ irreducible representation. At 0.5% tensile strain, this phonon mode is already hardened with a phase transition to the tetragonal ferroelectric structure with the $Amm2$ symmetry and lowest phonon frequencies of A_1, B_1, and B_2 are presented in Figure 1. The full band diagram of unstrained $KTaO_3$ (Figure S1) and under −2.1 % strain (Figure S2) can be found in the Supporting Information Section I. The exact strain value that this transition occurs strongly depends on the exchange and correlational functional choice of DFT. Here, we choose the PBEsol functional because it is stable at the $Pm\bar{3}m$ structure, in agreement with the literature [36], allowing us to study the effects of strain separately, while the SCAN functional is not stable and quantum anharmonic effects play a significant role in $KTaO_3$, which is beyond the scope of this manuscript [37, 38].

2.2 | Growth and Structural Characterization

$KTaO_3$ grows "cube-on-cube" on $SrTiO_3$ (001) substrates and "cube-on-pseudocube" on $DyScO_3$ $(110)_o$ (pseudo-cubic lattice-constant 3.947 Å [39], where the subscript O indicates orthorhombic indices) and $GdScO_3$ $(110)_o$ (pseudo-cubic lattice-constant 3.967Å [39]). The MBE growth details are described elsewhere [30]. Here, all the films are grown in an adsorption-controlled regime with a K:Ta excess flux ratio of about 10:1. X-ray diffraction (XRD) was used to characterize the structural quality of grown films. XRD of the $KTaO_3/SrTiO_3$ film is shown in Figure 2a; the $KTaO_3/DyScO_3$ and $KTaO_3/GdScO_3$ samples are shown in the Supporting Information (Figure S3). The θ–2θ scan shows only 001 peaks, confirming that the film is single-phase and oriented with its c-axis perpendicular to the plane of the substrate.

X-ray reciprocal space mapping (RSM) around $SrTiO_3$ and $KTaO_3$ 103 reflections confirm that the films are coherently strained to the substrate (Figure 2b). The full width at half maximum (FWHM) of the rocking curve of the $KTaO_3$ ($\Delta\omega \approx 0.008°$) film is as narrow as the $SrTiO_3$ substrate ($\Delta\omega \approx 0.007°$), suggesting high crystalline quality of the grown layers (Figure 2c). The films grown on $GdScO_3$ and $DyScO_3$ both show comparable FWHM values along both orthogonal in-plane directions of the substrate (Figures S5 and S6).

Thermodynamic analysis was applied to compare the out-of-plane lattice constant c_{KTO} of commensurately strained $KTaO_3$ films on different mismatched substrates, using the paraelectric and ferroelectric ground states of $KTaO_3$ (Figure 2d). The solid lines are calculated using a single set of coefficients (Tables S2 and S3). The out-of-plane lattice constant of the strained $KTaO_3$ films were determined from the 00ℓ (ℓ=1,2,3) reflection peaks and the full diffraction spectra, described in the Supporting Information III. The calculated out-of-plane lattice constant, expected for a commensurately strained $KTaO_3$ thin film on $SrTiO_3$ at room temperature is 4.028 Å, assuming a paraelectric ground state. XRD resolves an out-of-plane lattice constant of 4.063 ± 0.005 Å for the $KTaO_3$ film, grown commensurate to the $SrTiO_3$ (001) substrate. The discrepancy between the measured and calculated out-of-plane lattice parameters could be due to a structural phase transition with epitaxial strain. Figure 2d plots the calculated ferroelectric contribution to the out-of-plane lattice constant (orange region). Here, the measured out-of-plane lattice constant is consistent with the upper bound of the calculated ferroelectric contribution. The out-of-plane lattice constant becomes similar to the calculated value for the paraelectric ground state in partially relaxed films [30]. We also note a previous effort to grow $KTaO_3$ films commensurate to $SrTiO_3$ (001) using pulsed-laser epitaxy,

15214095, 2026, 57, Downloaded from https://advanced.onlinelibrary.wiley.com/doi/10.1002/adma.74366, Wiley Online Library on [16/11/2026]. See the Terms and Conditions (https://onlinelibrary.wiley.com/terms-and-conditions) on Wiley Online Library for rules of use; OA articles are governed by the applicable Creative Commons License

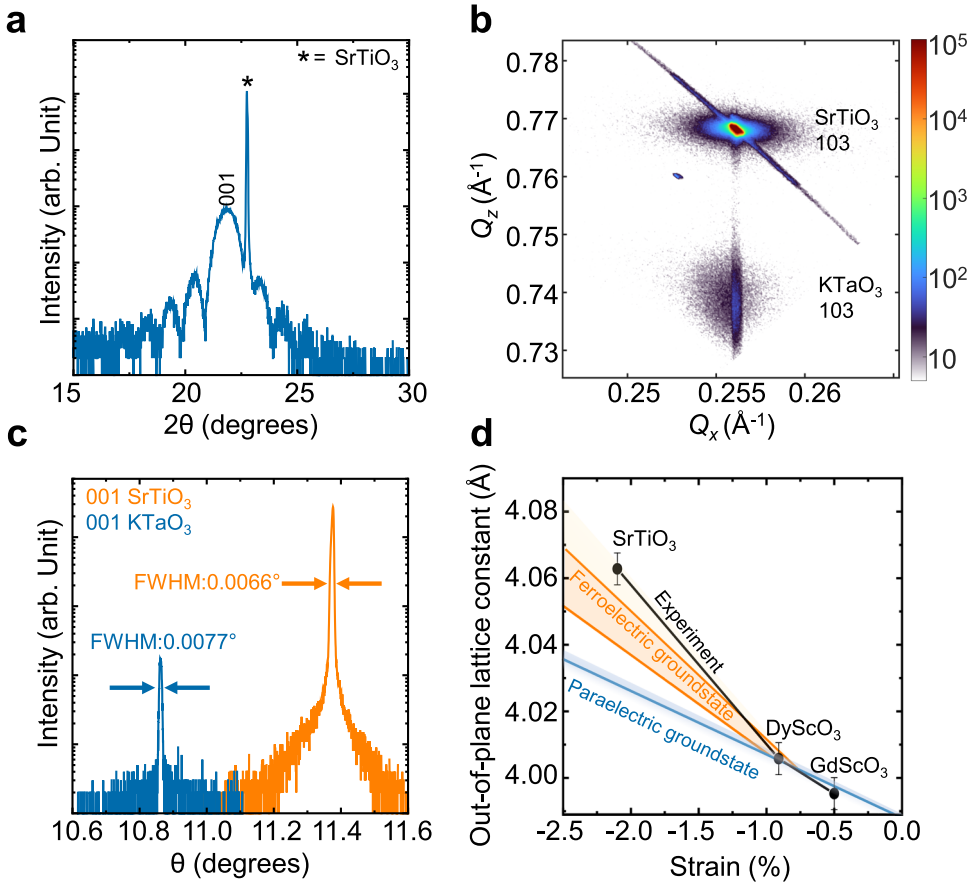


FIGURE 2 | X-Ray diffraction of a 9.3 nm thick film of $KTaO_3$ grown on $SrTiO_3$ (001). (a) θ–2θ scan showing the 001 reflection of $KTaO_3$ and $SrTiO_3$. Symmetric Laue fringes indicate a well-defined film thickness, indicative of an abrupt interface between film and substrate (asterisks * denotes substrate reflections). (b) X-ray reciprocal space mapping of the same 9.3 nm thick $KTaO_3$ film, confirming that the film is commensurately strained to the $SrTiO_3$ substrate. (c) Overlaid rocking curves of the 001 $KTaO_3$ and $SrTiO_3$ peaks, showing comparable FWHMs, indicating low out-of-plane mosaicity ($\Delta\omega \approx 0.008°$). (d) Measured out-of-plane lattice constant of $KTaO_3$ thin films on various substrates against the expected lattice constants from thermodynamic analysis of the paraelectric (blue) and the ferroelectric (orange) ground states. The range in the calculated out-of-plane lattice constant is due to the range in the reported sets of coefficients (Tables S2 and S3).

reporting a 4.008 ± 0.0005 Å out-of-plane lattice constant for $KTaO_3$ films [33]. Our results differ significantly from the previous study. The improved composition and structural perfection, achieved through adsorption-controlled growth, suggest that our results reflect the intrinsic behavior of $KTaO_3$.

In contrast to the extended out-of-plane lattice spacing observed for the commensurately strained $KTaO_3$ films grown on a $SrTiO_3$ substrate, the 18 nm thick $KTaO_3$ film on $DyScO_3$ and the 18 nm thick film on $GdScO_3$ appear consistent with the thermodynamic predictions for a paraelectric phase. Atomic force microscopy (AFM) micrographs (Figure S4) reveal a root-mean-square (rms) roughness for the 9.3 nm thick $KTaO_3$ on $SrTiO_3$ of ≈ 0.8 nm, measured by taking a 5 μm^2 area as a reference. For the $KTaO_3$ thin films grown on $DyScO_3$ and $GdScO_3$, the rms are 0.9 and 0.6 nm, respectively (see Figures S5 and S6).

HAADF-STEM was used to further investigate the polar distortions in the $KTaO_3$ films. Figure 3a,b displays HAADF-STEM images of the $KTaO_3$ film grown on a $SrTiO_3$ substrate. The interface between $KTaO_3$ and $SrTiO_3$ is sharp, and the film remains coherently strained to the substrate, indicating a high-quality epitaxial relationship between the two materials. Figure 3a also includes a zoomed-in region of the $KTaO_3$ film, presented in false color to highlight the displacement of the K column relative to the surrounding Ta columns. The accompanying schematic illustrates the definition of the displacement vector. The displacement vector is defined as the position of the Gaussian-fitted K-column relative to the centroid of the four Gaussian-fitted neighboring Ta-column positions, $d = \mathbf{r}_K - \mathbf{r}_{Ta-centroid}$. Displacements along the [001] direction (d_z) and [100] direction (d_x) were extracted to quantify the local polar distortion. Figure 3c shows the resulting displacement vector field overlaid on the HAADF-STEM image. Polar displacements are negligible in the $SrTiO_3$ substrate, whereas significant displacements are observed in the $KTaO_3$ film, which we attribute to strain-induced polarization. For a more robust analysis, we examined over 20 000 columns from multiple samples. Figure 3d presents the pooled distribution of displacements along the [001] and [100] crystallographic directions, revealing that the displacements are predominantly aligned along [001], consistent with a preferential out-of-plane polarization as predicted theoretically (Figure 1). Figure 3e

15214095, 2026, 57, Downloaded from https://advanced.onlinelibrary.wiley.com/doi/10.1002/adma.74366, Wiley Online Library on [16/11/2026]. See the Terms and Conditions (https://onlinelibrary.wiley.com/terms-and-conditions) on Wiley Online Library for rules of use; OA articles are governed by the applicable Creative Commons License

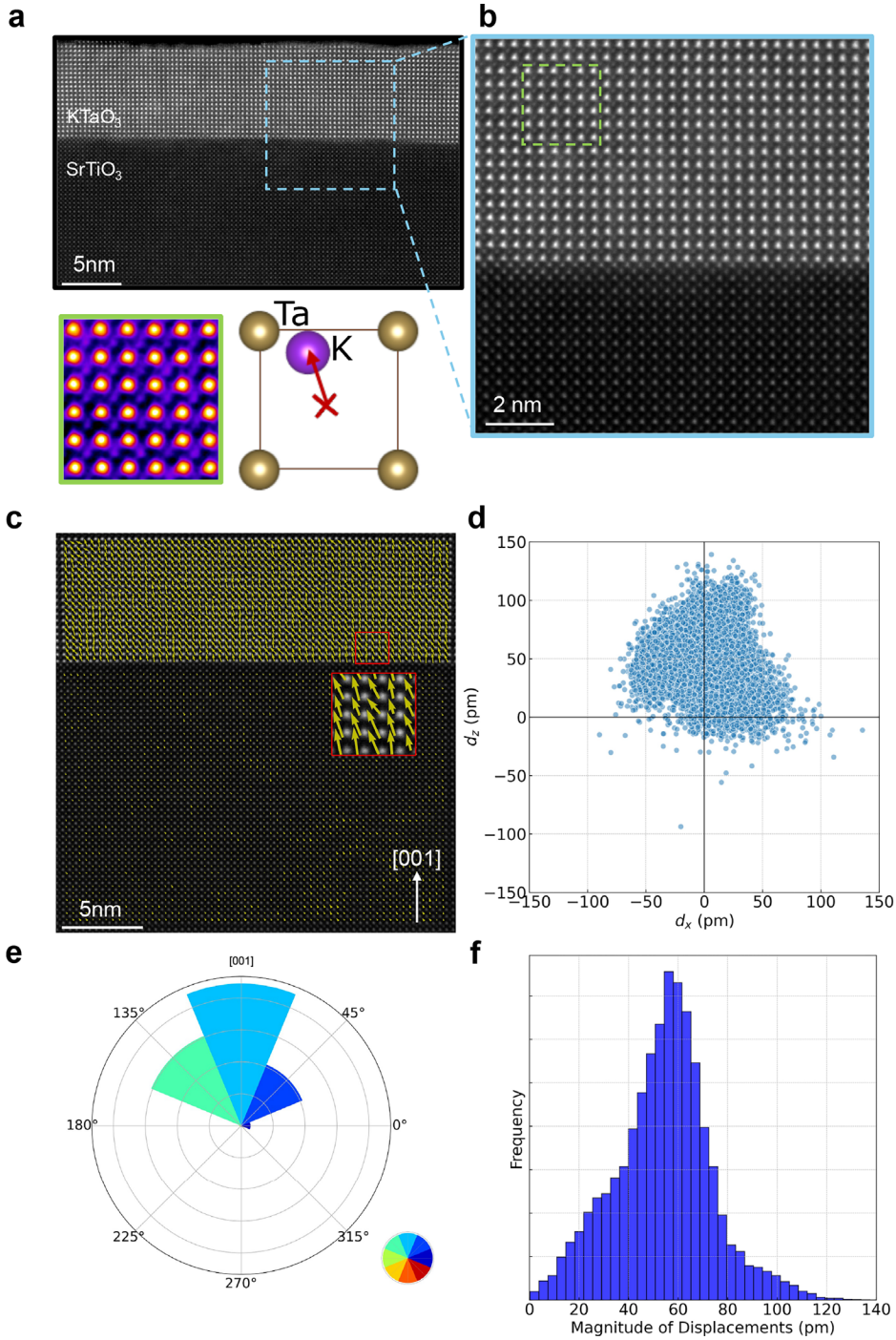


FIGURE 3 | Probing the polar distortions at the atomic scale in epitaxially strained $KTaO_3$. (a) HAADF-STEM image of the $KTaO_3$ film grown on $SrTiO_3$(001). (b) The interface structure is uniform throughout the sample, indicating a coherent strain between the film and the substrate. No extended defects are observed, which suggests high-quality epitaxial growth. (c) Displacement vectors of K columns relative to the centroid of the four neighboring Ta columns, overlaid on the HAADF-STEM image. The K and Ta column positions are obtained by 2D Gaussian fitting, and arrow lengths are scaled for visibility. (d) Tracing of the magnitude and direction of the displacements of atomic columns. (e) Polar histogram, based on more then 20 000 analyzed columns, shows the overall direction of displacements for the $KTaO_3$ thin film grown on a $SrTiO_3$ substrate. (f) Histogram of the magnitude of the polar displacements in potassium columns, based on the 20 000 columns analyzed.

shows the polar histogram of displacement directions, further confirming that the polar displacements are primarily aligned along [001]. Additional two-dimensional statistical analysis of the pooled displacement distributions for $KTaO_3$ films grown on $SrTiO_3$, $DyScO_3$, and $GdScO_3$, as well as for the $DyScO_3$-based switched metal–insulator–metal (MIM) heterostructure, is provided in Supporting Information Section V. While the film on $DyScO_3$ (Figure S9) shows a slight net out-of-plane polar displacement, the film on $GdScO_3$ (Figure S11) shows no net out-of-plane displacement, with average $d_z = -1.2$ pm, but does show a finite in-plane mean displacement, with average $d_x = -12.3$ pm. We distinguish this finite in-plane displacement from the

15214095, 2026, 57, Downloaded from https://advanced.onlinelibrary.wiley.com/doi/10.1002/adma.74366, Wiley Online Library on [16/11/2026]. See the Terms and Conditions (https://onlinelibrary.wiley.com/terms-and-conditions) on Wiley Online Library for rules of use; OA articles are governed by the applicable Creative Commons License

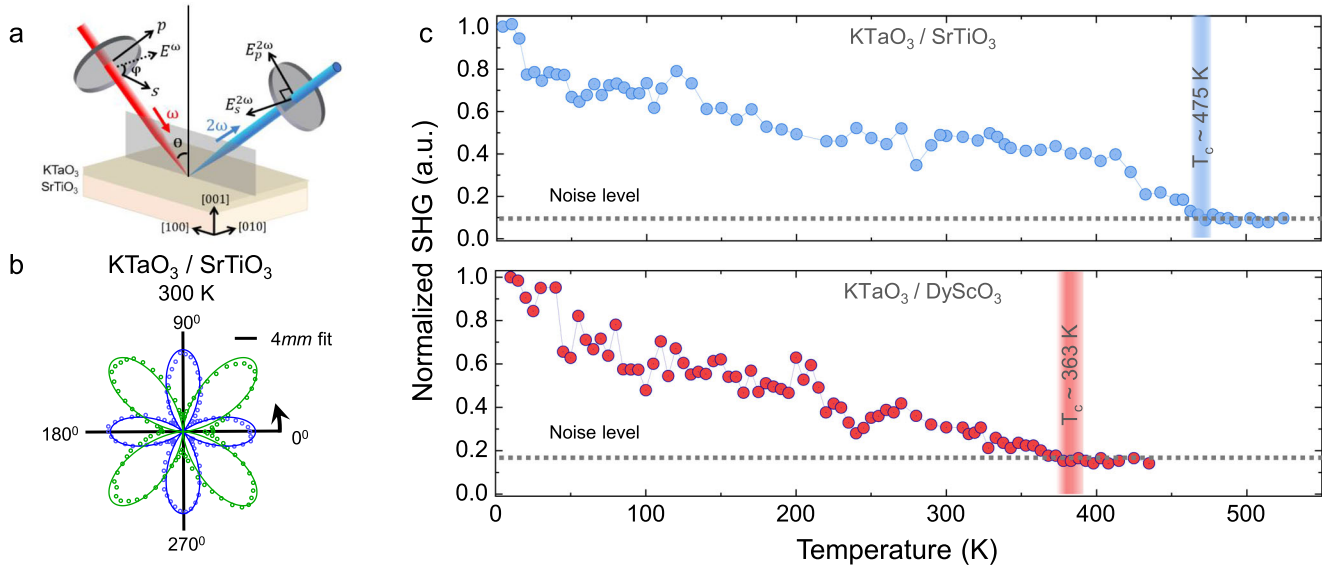


FIGURE 4 | Emergence of the polar *P4mm* space group in epitaxially strained $KTaO_3$. (a) Schematic of SHG setup in reflection geometry. (b) Polar plots of SHG intensity (radius) versus fundamental polarization (azimuth). (c) Normal and oblique incidence SHG intensity with temperature (10–550 K), shown for the 9.3 nm thick $KTaO_3$ film grown on $SrTiO_3$ and an 18 nm-thick $KTaO_3$ film grown on $DyScO_3$.

strain-induced out-of-plane tetragonal polar state discussed here, as described in Supporting Information Section V. In addition, HAADF-STEM performed on the $DyScO_3$-based epitaxial MIM heterostructure that exhibits ferroelectric switching reveals a clear nonzero mean out-of-plane displacement in the active device region, consistent with a predominantly out-of-plane polar state (Figure S10). Figure 3f exhibits the distribution of the K-column displacement magnitude. The average magnitude of the polar displacements is 54.08 ± 19.75 pm. This distribution highlights the significant atomic displacements occurring in the $KTaO_3$ film due to epitaxial strain. For small distortions, the change in polarization is linear in the atomic displacements. We estimate the spontaneous polarization (P_s) using the following relationship:

$$P_s = \frac{e}{V_{KTO}} \sum_i Z_i^* \times u_i, \tag{3}$$

where e is the elementary charge, V_{KTO} is the unit cell volume of $KTaO_3$, Z_i^* the Born-effective charge (BEC) tensor coefficient and u_i is the polar atomic distortions. The calculated BEC tensor can be found in Supporting Information VI. Equation (3) sums the contributions of all the ions in the unit cell to spontaneous polarization. Here, only considering the polar distortions from potassium columns, resolved from room temperature HAADF-STEM, estimates the spontaneous polarization of $P_s = 18 \pm 6\,\mu C\,cm^{-2}$.

2.3 | Probing the Emergence of Ferroelectricity

SHG measurements as a function of temperature were performed for the previously described $KTaO_3/SrTiO_3$, $KTaO_3/DyScO_3$, and $KTaO_3/GdScO_3$ samples. A schematic of the SHG setup used for the experiment is illustrated in Figure 4a. SHG detects a signal that exceeds that of $SrTiO_3$ substrate, indicating the long-range breaking of inversion symmetry. By rotating the polarization of the incident beam, polar plots can be generated, corresponding to *p*- and *s*-polarized SHG light reflected off the sample. The derivation of the fitting model is further elaborated in the Supporting Information VII. For the largest in-plane compressive strain $KTaO_3/SrTiO_3$ sample (−2.1%) the phase transition temperature is at 475 K, while for the $KTaO_3/DyScO_3$ (−0.9%) samples a polar phase is detected below 360 K. For temperatures below T_C, the strained $KTaO_3$ films display the same tetragonal average symmetry, as shown in Figure 4b, suggesting the absence of any other symmetry-lowering phase transitions.

If $KTaO_3$ films on $SrTiO_3$ exceed the critical thickness, resulting in strain relaxation, no SHG intensity is detected beyond that of the substrate (see Supporting Information VIII). Rotational anisotropy SHG results are successfully fitted to the *4mm* point group, further solidifying the emergence of a polar phase (Figure 4b), consistent with HAADF-STEM and XRD measurements. Although SHG confirms the emergence of spontaneous electric polarization, it is necessary to exhibit switching of polarization to confirm ferroelectricity.

We note the discrepancy between thermodynamic calculations and experimental evidence, XRD (Figure 2d), HAADF-STEM (Figure S11), and SHG (Figure 4c) for the $KTaO_3$ films grown on $GdScO_3$. Here, thermodynamic calculations suggest the emergence of a polar phase at around 100 K, while SHG does not show signal at any temperatures down to 4 K. To further support this observation, SHG intensity was measured as a function of incident beam fluence, which shows no measurable difference between $KTaO_3/GdScO_3$ and a bare $GdScO_3$ substrate at room and low temperatures (Figure S13c). The out-of-plane lattice parameter from XRD (Figure 2d) and the out-of-plane displacement extracted from HAADF-STEM (Figure S11) also show no out-of-plane polar order in $KTaO_3/GdScO_3$ heterostructure at room temperature. These results suggest that a threshold strain must be applied to stabilize the polar phase. DFT calculations also support a critical epitaxial strain for emergence of

15214095, 2026, 57, Downloaded from https://advanced.onlinelibrary.wiley.com/doi/10.1002/adma.74366, Wiley Online Library on [16/11/2026]. See the Terms and Conditions (https://onlinelibrary.wiley.com/terms-and-conditions) on Wiley Online Library for rules of use; OA articles are governed by the applicable Creative Commons License

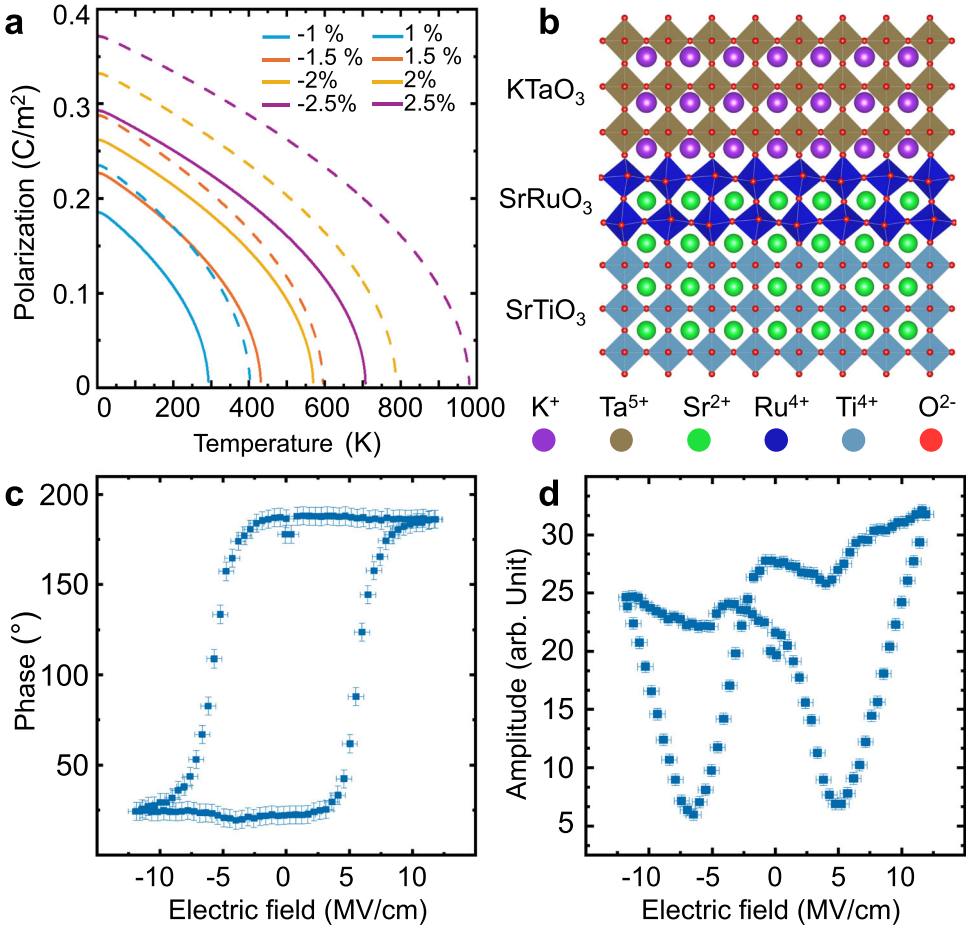


FIGURE 5 | Switching of spontaneous electric polarization in epitaxially strained $KTaO_3$. (a) Thermodynamic calculation of the polarization as a function of epitaxial strain and temperature. (b) Schematic of the epitaxial heterostructure used for PFM measurements. (c) PFM-resolved hysteresis loop of $KTaO_3/SrRuO_3/SrTiO_3$ heterostructure, confirming electric switching of spontaneous electric polarization. (d) Magnitude of the piezo response.

ferroelectricity (Figure 1b). The DFT-resolved critical epitaxial strain for ferroelectric transition, however, depends on the exchange and correlational functional choices and could only qualitatively support the critical strain for ferroelectric transition.

Figure 5a shows phase-field simulation results, estimating the spontaneous polarization in $KTaO_3$ with strain and temperature. Under epitaxial strain of –2.1%, as imposed by coherent growth on $SrTiO_3$, the spontaneous polarization reaches $\sim 26\,\mu C\,cm^{-2}$ at liquid helium temperature. The predicted room temperature electric polarization is $\sim 19\,\mu C\,cm^{-2}$, which is consistent with the STEM-resolved polarization ($18 \pm 6\,\mu C\,cm^{-2}$) using Equation (3). We note reports of oxygen octahedra distortions under strain [40] and potassium desorption [41] in $KTaO_3$. Furthermore, significant anion contributions to spontaneous polarization is reported in $NaNbO_3$ [42]. Here, the cation polar distortions, unlike $NaNbO_3$, are significant and their contribution alone could explain the calculated spontaneous polarization, suggesting that anion contributions to electric polarization are negligible.

To determine whether this strain-induced electric polarization is switchable under applied electric field, a capacitor stack was fabricated: $KTaO_3$ grown on a conductive $SrRuO_3$ bottom electrode on $SrTiO_3$ (001). For structural details, see Supporting Information III. Local electromechanical measurements using piezoresponse force microscopy (PFM) were used to reveal ferroelectric switching and the hysteresis loop, instead of conventional PUND techniques, due to the leakage current that often dominates electrical measurements in ultrathin layers [43]. Figure 5b illustrates the heterostructure used for PFM: $KTaO_3/SrRuO_3/SrTiO_3$, where $SrRuO_3$ serves as an epitaxial bottom electrode. Clear 180° phase reversal for out-of-plane PFM response at an arbitrary location on the capacitors of $KTaO_3/SrRuO_3/SrTiO_3$ is shown in Figure 5c. At a quasi-static frequency of 1.1 Hz standard ferroelectric $d_{33} - V$ is observed with coercive voltages of ± 5.7 V. The error bars represent the average response over the 10 cycles of a "pulse-mode" triangular wave. The butterfly-shaped amplitude curve confirms ferroelectric switching (Figure 5d). Additionally, $KTaO_3/SrRuO_3/DyScO_3$ capacitor heterostructure was investigated using PFM. A 180° phase reversal for the out-of-plane PFM response is observed (Figure S14). This result is consistent with thermodynamic calculations (Figure 1a) and SHG (Figure 4b), exhibiting an above room temperature polar transition. The $KTaO_3$ films grown on $DyScO_3$, however, do not demonstrate an extended XRD lattice constant (Figure 2d) and HAADF-STEM shows a small net out-of-plane polar distortion (Figure S9). This could be due to the presence of polar nanoregions and an order–disorder ferroelectric transition, which has been reported in strained $SrTiO_3$ films [44–46]. The switched MIM test structures commensurate to $DyScO_3$, on the other hand,

15214095, 2026, 57, Downloaded from https://advanced.onlinelibrary.wiley.com/doi/10.1002/adma.74366, Wiley Online Library on [16/11/2026]. See the Terms and Conditions (https://onlinelibrary.wiley.com/terms-and-conditions) on Wiley Online Library for rules of use; OA articles are governed by the applicable Creative Commons License

exhibit a significant enhancement of out-of-plane polar distortion in HAADF-STEM compared to the film grown directly on $DyScO_3$ (Figure S10). Finally, we do not observe any polar switching behavior in similar heterostructures grown on $GdScO_3$.

In conclusion, high-quality $KTaO_3$ thin films were coherently strained to various substrates exerting a compressive in-plane strain ranging from -0.5% on $GdScO_3$ up to −2.1% on $SrTiO_3$. The emergence of a tetragonal polar *P*4*mm* phase is predicted by DFT and thermodynamic calculations and experimentally confirmed by diffraction, SHG, and HAADF-STEM. We demonstrated the switching of the emergent spontaneous electric polarization using PFM. The room temperature phase-field spontaneous polarization (19 μCcm^{-2}) is consistent with the experimentally resolved value (18 ± 6 $\mu C\ cm^{-2}$) using HAADF-STEM atomic polar distortions and calculated BEC tensor. We have thus revealed a ferroelectric ground state in epitaxially strained $KTaO_3$.

Given the recent discovery of unconventional superconductivity at $KTaO_3$ interfaces [21, 47, 48] and reports of ferroelectric enhancement of superconductivity [28, 29, 49], tunable ferroelectricity in $KTaO_3$ provides a platform for evaluating theoretical proposals that link superconductivity to a proximal ferroelectric state [27, 50–52].

3 | Methods

3.1 | Thin Film Synthesis and Characterization

Epitaxial $KTaO_3$ films were grown in a modified Vecco GEN 10 MBE system. The substrate was heated using a 10 μm CO_2-laser, Epiray GmbH (THERMALAS Substrate Heater). Films were grown by co-deposition of potassium, tantalum, and ozone at a substrate temperature of 650 °C, measured using an optical pyrometer operating at a 7.5 μm wavelength. Here, all the films were grown in an adsorption-controlled regime with a K:Ta flux ratio of approximately 10:1. A mixture of ozone and oxygen (10% O_3 + 90% O_2) was used as the oxidant. The films were grown at an oxidant background pressure of 1×10^{-6} Torr. Typical fluxes for the sources were $(4-7) \times 10^{12}$ atoms/cm^2/s for the tantalum source and $(4-7) \times 10^{13}$ atoms/cm^2/s for the potassium source, determined by a quartz crystal microbalance (QCM), with an accuracy of about ± 15%. Co-deposition with these fluxes results in a $KTaO_3$ film growth rate of about 0.03 Å/s. Additional MBE growth details are described elsewhere [30].

X-ray diffraction (XRD), x-ray reflectometry (XRR), and reciprocal space mapping (RSM) measurements were carried out using a PANalytical Empyrean diffractometer with Cu Kα_1 radiation. The raw XRR spectra were analyzed using the PANalytical X'Pert Reflectivity software package and the layer thickness was derived from a fast Fourier transform (FFT) after manually defining the critical angle to account for refractive effects. In situ reflection high-energy electron diffraction (RHEED) patterns were recorded using kSA-400 software and a Staib electron source operated at 14 kV and a filament current of 1.5 A. The morphology of the film surface was characterized using an Asylum Cypher ES environmental AFM. Piezoforce microscopy (PFM) was conducted on an Asylum Cypher AFM using Dual AC Resonance Tracking (DART) mode.

3.2 | Transmission Electron Microcopy

Cross-sectional scanning transmission electron microscopy (STEM) samples were prepared using a standard lift-out process with a Thermo Fisher Scientific Helios G4 UX focused ion beam, with a final milling voltage of 2 kV for the Ga ions. Atomic-resolution HAADF-STEM images of the $KTaO_3/SrTiO_3$, $KTaO_3/DyScO_3$, and $KTaO_3/GdScO_3$ samples were acquired on a Thermo Fisher Scientific Spectra 300 X-CFEG operated at 200 kV with a convergence angle of 30 mrad and a HAADF detector collection range of 60–200 mrad. Additional cross-sectional STEM imaging of the $DyScO_3$-based capacitor heterostructure was performed at the Center for Electron Microscopy and Analysis (CEMAS) at The Ohio State University using a Thermo Fisher Scientific Themis Z microscope operated at 200 kV with a probe semi-convergence angle of 20 mrad and a HAADF detector collection range of 64–200 mrad. To improve signal-to-noise ratio, 25 fast-scan images (2048 × 2048 pixels, 200 ns dwell time) were aligned and averaged. Atomic column positions were first identified automatically using Atomap, followed by nearest-neighbor assignment. The positions were then refined in two steps: first by center-of-mass refinement and subsequently by 2D Gaussian fitting of the column intensities. The displacement of each K column was then calculated relative to the centroid of the four neighboring Ta columns.

3.3 | Second-Harmonic Generation

Second-harmonic generation (SHG) measurements were made with an 800 nm fundamental wavelength pulsed laser line from a Spectra-Physics Solstice Ace laser focused on the sample, while second-harmonic light generated at 400 nm was measured reflecting off the samples. The repetition rate of the laser was 1 kHz, while the beam size at focus was 16 μm. All measurements were done in reflection geometry. For low temperature measurements, a Janis 30 gas flow cryostat was used, while for high-temperature measurements, a homemade heater was employed.

3.4 | Density Functional Theory

The atomic structure relaxation, phonon, and Berry phase calculations were performed using first-principles density functional theory within the generalized gradient approximation (GGA) as implemented in the PBEsol functional [53] by the Vienna Ab initio Simulation Package (VASP) [54] with the ion–electron interaction described by the projector augmented wave method [55] including the spin-orbit coupling (SOC) effects. We employed an energy cutoff of 700 eV, Gaussian smearing of 0.005 eV, and electronic energy tolerance of 10^{-8} eV for the total energy convergence. The ionic relaxations were performed with a force tolerance of 10^{-3} Å/eV and an electronic momentum *k*-point mesh of 24 × 24 × 24. Phonon and Berry phase calculations were performed with an electronic momentum *k*-point mesh of 16 × 16 × 16. Phonon calculations were analyzed using the Phonopy code [56].

15214095, 2026, 57, Downloaded from https://advanced.onlinelibrary.wiley.com/doi/10.1002/adma.74366, Wiley Online Library on [16/11/2026]. See the Terms and Conditions (https://onlinelibrary.wiley.com/terms-and-conditions) on Wiley Online Library for rules of use; OA articles are governed by the applicable Creative Commons License

3.5 | Thermodynamics

Using Landau–Ginzburg–Devonshire theory for ferroelectrics, the elastic Gibbs free energy density g, written as a power series of the polarization near the phase transition (Supporting Information Discussion II), describes the ferroelectric phase transition [57]. The ferroelectic transition temperature can be calculated by solving Equations (1) and (2), which allows the construct of the phase transition boundaries between the paraelectric and ferroelectric phases in the temperature-strain phase diagram. Since there is some variation in the data collected on the electrostrictive coefficients and elastic constants from the literature, we list the values by different groups in Tables S2 and S3 and include the regions indicating the range of ferroelectric transition to account for the spread in these values exhibited in Figure 1a.

Acknowledgements

K.A. is supported by the U.S. National Science Foundation under Grant No. NSF DMR-2408890. K.A. also acknowledges a seed grant from the Center for Emergent Materials, an NSF MRSEC, under Grant No. DMR-2011876. This material is based upon work supported by the National Science Foundation (Platform for the Accelerated Realization, Analysis, and Discovery of Interface Materials (PARADIM)) under Cooperative Agreement No. DMR-2039380. S.H., A.R., L-Q.C., and V.G. acknowledge support from the National Science Foundation grant DMREF DMR-2011839 for SHG characterization and phase-field modeling. A.R. acknowledges the support of the National Science Foundation Graduate Research Fellowship Program under Grant No. DGE1255832. U.S. was supported by the U.S. Department of Energy, Office of Science, Basic Energy Sciences under grant number DE-SC-0012375. This work made use of a Helios FIB supported by NSF (Grant No. DMR-1539918) and the Cornell Center for Materials Research (CCMR) Shared Facilities, which are supported through the NSF MRSEC Program (Grant No. DMR-1719875). The authors acknowledge Steve Button for substrate preparation. We gratefully acknowledge Dasol Yoon and Xiyue Zhang for providing EDX analysis code.

Conflicts of Interest

The authors declare no conflicts of interest.

Data Availability Statement

The data that support the findings of this study are available within the article. Additional data related to film growth and structural characterization by XRD and STEM are available at https://doi.org/10.34863/1a2q-0380.

References

1. L. D. Nguyen, A. S. Brown, M. A. Thompson, and L. M. Jelloian, "50-nm Self-Aligned-Gate Pseudomorphic AlInAs/GaInAs High Electron Mobility Transistors," *IEEE Transactions on Electron Devices* 39, no. 9 (1992): 2007–2014.

2. R. Beach, J. Borchers, A. Matheny, et al., "Enhanced Curie temperatures and Magnetoelastic Domains in Dy/Lu Superlattices and Films," *Physical Review Letters* 70, no. 22 (1993): 3502.

3. D. Fuchs, E. Arac, C. Pinta, S. Schuppler, R. Schneider, and H. V. Löhneysen, "Tuning the Magnetic Properties of $LaCoO_3$ Thin Films by Epitaxial Strain," *Physical Review B* 77, no. 1 (2008): 014434.

4. K. J. Choi, M. Biegalski, Y. Li, A. Sharan, et al., "Enhancement of Ferroelectricity in Strained $BaTiO_3$ Thin Films," *Science* 306, no. 5698 (2004): 1005–1009.

5. I. Bozovic, G. Logvenov, I. Belca, B. Narimbetov, and I. Sveklo, "Epitaxial Strain and Superconductivity in $La_{2-x}Sr_xCuO_4$ Thin Films," *Physical Review Letters* 89, no. 10 (2002): 107001.

6. J. H. Lee, L. Fang, E. Vlahos, et al., "A Strong Ferroelectric Ferromagnet Created by Means of Spin–Lattice Coupling," *Nature* 466, no. 7309 (2010): 954–958.

7. J. Haeni, P. Irvin, W. Chang, et al., "Room-Temperature Ferroelectricity in Strained $SrTiO_3$," *Nature* 430, no. 7001 (2004): 758–761.

8. J. P. Ruf, H. Paik, N. J. Schreiber, et al., "Strain-Stabilized Superconductivity," *Nature Communications* 12, no. 1 (2021): 59.

9. J. F. Scott and C. A. Paz de Araujo, "Ferroelectric Memories," *Science* 246, no. 4936 (1989): 1400–1405.

10. A. Devonshire, "Theory of ferroelectrics," *Advances in Physics* 3, no. 10 (1954): 85–130.

11. N. Pertsev, A. Zembilgotov, and A. Tagantsev, "Effect of Mechanical Boundary Conditions on Phase Diagrams of Epitaxial Ferroelectric Thin Films," *Physical Review Letters* 80, no. 9 (1998): 1988.

12. M. Biegalski, "Epitaxialy Strained Strontium Titante," (PhD Thesis, The Pennsylvania State University, 2006), 97–123, https://etda.libraries.psu.edu/catalog/6919.

13. G. Sheng, Y. Li, J. Zhang, et al., "A Modified Landau–Devonshire Thermodynamic Potential for Strontium Titanate," *Applied Physics Letters* 96, no. 23 (2010): 232902.

14. H. Uwe and T. Sakudo, "Electrostriction and Stress-Induced Ferroelectricity in $KTaO_3$," *Journal of the Physical Society of Japan* 38, no. 1 (1975): 183–189.

15. S. Hazra, T. Schwaigert, A. Ross, et al., "Colossal Strain Tuning of Ferroelectric Transitions in $KNbO_3$ Thin Films," *Advanced Materials* 36, no. 52 (2024): 2408664.

16. H. Nakamura and T. Kimura, "Electric Field Tuning of Spin-Orbit Coupling in $KTaO_3$ Field-Effect Transistors," *Physical Review B* 80, no. 12 (2009): 121308.

17. A. Gupta, H. Silotia, A. Kumari, et al., "$KTaO_3$–the new Kid on the Spintronics Block," *Advanced Materials* 34, no. 9 (2022): 2106481.

18. K. Zou, S. Ismail-Beigi, K. Kisslinger, et al., "$LaTiO_3/KTaO_3$ Interfaces: A New Two-Dimensional Electron Gas System," *APL Materials* 3, no. 3 (2015): 036104.

19. A. H. Al-Tawhid, D. P. Kumah, and K. Ahadi, "Two-Dimensional Electron Systems and Interfacial Coupling in $LaCrO_3/KTaO_3$ Heterostructures," *Applied Physics Letters* 118, no. 19 (2021): 192905.

20. A. H. Al-Tawhid, J. Kanter, M. Hatefipour, D. P. Kumah, J. Shabani, and K. Ahadi, "Superconductivity and Weak Anti-Localization at $KTaO_3$ (111) Interfaces: Ah Al-Tawhid et al.," *Journal of Electronic Materials* 51, no. 11 (2022): 6305–6309.

21. C. Liu, X. Yan, D. Jin, et al., "Two-Dimensional Superconductivity and Anisotropic Transport at $KTaO_3$ (111) Interfaces," *Science* 371, no. 6530 (2021): 716–721.

22. E. G. Arnault, A. H. Al-Tawhid, S. Salmani-Rezaie, et al., "Anisotropic Superconductivity at $KTaO_3$(111) Interfaces," *Science Advances* 9, no. 7 (2023): eadf1414.

23. S. J. Poage, X. Gao, M. Baksi, et al., "Violation of the Pauli Limit at $KTaO_3$(110) Interfaces," *Physical Review B* 111 (2025): 214506.

24. L. M. Vicente-Arche, J. Bréhin, S. Varotto, et al., "Spin–Charge Interconversion in $KTaO_3$ 2D Electron Gases," *Advanced Materials* 33, no. 43 (2021): 2102102.

25. A. H. Al-Tawhid, R. Sun, A. H. Comstock, D. P. Kumah, D. Sun, and K. Ahadi, "Spin-to-Charge Conversion at $KTaO_3$ (111) Interfaces," *Applied Physics Letters* 126, no. 9 (2025): 091601.

15214095, 2026, 57, Downloaded from https://advanced.onlinelibrary.wiley.com/doi/10.1002/adma.74366, Wiley Online Library on [16/11/2026]. See the Terms and Conditions (https://onlinelibrary.wiley.com/terms-and-conditions) on Wiley Online Library for rules of use; OA articles are governed by the applicable Creative Commons License

26. N. Wu, X.-J. Zhang, and B.-G. Liu, "Strain-Enhanced Giant Rashba Spin Splitting in Ultrathin $KTaO_3$ Films for Spin-Polarized Photocurrents," *RSC Advances* 10, no. 72 (2020): 44088–44095.

27. F. Yang and L. Chen, "Ferroelectric Order and Enhanced Interfacial Superconductivity in Lightly-Doped Quantum Paraelectric $KTa_{1-x}Nb_xO_3$," preprint, arXiv, November 11, 2025, arXiv:2511.08253.

28. K. Ahadi, L. Galletti, Y. Li, S. Salmani-Rezaie, W. Wu, and S. Stemmer, "Enhancing Superconductivity in $SrTiO_3$ Films With Strain," *Science Advances* 5, no. 4 (2019): eaaw0120.

29. R. Russell, N. Ratcliff, K. Ahadi, L. Dong, S. Stemmer, and J. W. Harter, "Ferroelectric Enhancement of Superconductivity in Compressively Strained $SrTiO_3$ Films," *Physical Review Materials* 3 (2019): 091401.

30. T. Schwaigert, S. Salmani-Rezaie, M. R. Barone, et al., "Molecular Beam Epitaxy of $KTaO_3$," *Journal of Vacuum Science & Technology A* 41, no. 2 (2023): 022703.

31. J. Kim, M. Yu, J.-W. Lee, et al., "Electronic-Grade Epitaxial (111) $KTaO_3$ Heterostructures," *Science Advances* 10, no. 21 (2024): eadk4288.

32. L. Tao and J. Wang, "Strain-Tunable Ferroelectricity and Its Control of Rashba Effect in $KTaO_3$," *Journal of Applied Physics* 120, no. 23 (2016): 234101.

33. M. Tyunina, J. Narkilahti, M. Plekh, et al., "Evidence for Strain-Induced Ferroelectric Order in Epitaxial Thin-Film $KTaO_3$," *Physical Review Letters* 104, no. 22 (2010): 227601.

34. E. A. Zhurova, Y. Ivanov, V. Zavodnik, and V. Tsirelson, "Electron Density and Atomic Displacements in $KTaO_3$," *Acta Crystallographica Section B: Structural Science, Crystal Engineering and Materials* 56, no. 4 (2000): 594–600.

35. Y. Li and L. Chen, "Temperature-Strain Phase Diagram for $BaTiO_3$ Thin Films," *Applied physics letters* 88, no. 7 (2006): 072905.

36. N. A. S. T. Esswein, "First-Principles Calculation of Electron-Phonon Coupling in Doped $KTaO_3$," *Open Research Europe* 3 (2023): 177.

37. L. Ranalli, C. Verdi, L. Monacelli, G. Kresse, M. Calandra, and C. Franchini, "Temperature-Dependent Anharmonic Phonons in Quantum Paraelectric $KTaO_3$ by First Principles and Machine-Learned Force Fields," *Advanced Quantum Technologies* 6, no. 4 (2023): 2200131.

38. L. Ranalli, C. Verdi, M. Zacharias, J. Even, F. Giustino, and C. Franchini, "Electron mobilities in $SrTiO_3$ and $KTaO_3$: Role of phonon anharmonicity, mass renormalization, and disorder," *Physical Review Materials* 8 (2024): 104603.

39. R. Uecker, B. Velickov, D. Klimm, et al., "Properties of Rare-Earth Scandate Single Crystals (Re= Nd-Dy)," *Journal of Crystal Growth* 310, no. 10 (2008): 2649–2658.

40. C. Liu, J. Zhang, Y. Li, et al., "Atomic-Scale Insights Into the Polar Surface of $KTaO_3$ (001)," *Nano Letters* 25, no. 49 (2025): 17091–17095.

41. Q. Du, T. Eldred, X. Xu, et al., "Directly Visualizing the Formation of Artificial Structures and Their Charge in Oxides by Electron Microscopy," *ACS Nano* 19, no. 40 (2025): 35692–35700.

42. H. Kp, R. Xu, K. Patel, et al., "Electron Ptychography Reveals a Ferroelectricity Dominated by Anion Displacements," *Nature Materials* 24, no. 9 (2025): 1433–1440.

43. M. Dawber, K. Rabe, and J. Scott, "Physics of Thin-Film Ferroelectric Oxides," *Reviews of Modern Physics* 77, no. 4 (2005): 1083–1130.

44. R. Xu, J. Huang, E. S. Barnard, et al., "Strain-Induced Room-Temperature Ferroelectricity in $SrTiO_3$ Membranes," *Nature Communications* 11, no. 1 (2020): 3141.

45. S. Salmani-Rezaie, K. Ahadi, W. M. Strickland, and S. Stemmer, "Order-Disorder Ferroelectric Transition of Strained $SrTiO_3$," *Physical Review Letters* 125 (2020): 087601.

46. S. Salmani-Rezaie, K. Ahadi, and S. Stemmer, "Polar Nanodomains in a Ferroelectric Superconductor," *Nano Letters* 20, no. 9 (2020): 6542–6547.

47. A. H. Al-Tawhid, S. J. Poage, S. Salmani-Rezaie, et al., "Enhanced Critical Field of Superconductivity at an Oxide Interface," *Nano Letters* 23, no. 15 (2023): 6944–6950.

48. J. T. McCourt, E. G. Arnault, M. Baksi, et al., "Electrostatic Control of Quantum Phases in $KTaO_3$-Based Planar Constrictions," *Nano Letters* 25, no. 45 (2025): 16091–16096.

49. J. Kim, M. Yu, A. Omran, et al., "Enhanced Superconductivity at Quantum-Critical $KTaO_3$ Interfaces," preprint, arXiv, November 17, 2025, arXiv:2511.12904.

50. N. F. Yuan and L. Fu, "Supercurrent Diode Effect and Finite-Momentum Superconductors," *Proceedings of the National Academy of Sciences* 119, no. 15 (2022): e2119548119.

51. K. Dunnett, A. Narayan, N. A. Spaldin, and A. V. Balatsky, "Strain and Ferroelectric Soft-Mode Induced Superconductivity in Strontium Titanate," *Physical Review B* 97 (2018): 144506.

52. M. N. Gastiasoro, M. E. Temperini, P. Barone, and J. Lorenzana, "Theory of Superconductivity Mediated by Rashba Coupling in Incipient Ferroelectrics," *Physical Review B* 105 (2022): 224503.

53. J. P. Perdew, A. Ruzsinszky, G. I. Csonka, et al., "Restoring the Density-Gradient Expansion for Exchange in Solids and Surfaces," *Physical Review Letters* 100 (2008): 136406.

54. G. Kresse and J. Furthmüller, "Efficient Iterative Schemes for Ab Initio Total-Energy Calculations Using a Plane-Wave Basis Set," *Physical Review B* 54 (1996): 11169–11186.

55. G. Kresse and D. Joubert, "From Ultrasoft Pseudopotentials to the Projector Augmented-Wave Method," *Physical Review B* 59 (1999): 1758–1775.

56. A. Togo, L. Chaput, T. Tadano, and I. Tanaka, "Implementation Strategies in Phonopy and Phono3py," *Journal of Physics: Condensed Matter* 35, no. 35 (2023): 353001.

57. M. J. Haun, E. Furman, S. Jang, H. McKinstry, and L. Cross, "Thermodynamic Theory of $PbTiO_3$," *Journal of Applied Physics* 62, no. 8 (1987): 3331–3338.

Supporting Information

Additional supporting information can be found online in the Supporting Information section.

Supporting File: adma74366-sup-0001-SuppMat.pdf.

15214095, 2026, 57, Downloaded from https://advanced.onlinelibrary.wiley.com/doi/10.1002/adma.74366, Wiley Online Library on [16/11/2026]. See the Terms and Conditions (https://onlinelibrary.wiley.com/terms-and-conditions) on Wiley Online Library for rules of use; OA articles are governed by the applicable Creative Commons License

Above Room Temperature Ferroelectricity in Epitaxially Strained $KTaO_3$

Tobias Schwaigert,[1,2,a)] Salva Salmani-Rezaie,[3,4,a)] Sankalpa Hazra,[5,a)] Utkarsh Saha,[5] Maya Ramesh,[2] Aiden Ross,[5] Betül Pamuk,[6] Long-Qing Chen,[5] David A. Muller,[3,4] Darrell G. Schlom,[1,2,4,7] Venkatraman Gopalan,[5,8] and Kaveh Ahadi[9,10,b)]

[1)] *Platform for the Accelerated Realization, Analysis, and Discovery of Interface Materials (PARADIM), Cornell University, Ithaca, New York 14853, USA*

[2)] *Department of Materials Science and Engineering, Cornell University, Ithaca, NY 14853, USA*

[3)] *School of Applied and Engineering Physics, Cornell University, Ithaca, New York 14853, USA*

[4)] *Kavli Institute at Cornell for Nanoscale Science, Cornell University, Ithaca, New York 14853, USA*

[5)] *Material Science and Engineering, Pennsylvania State University, University Park, PA 16802, USA*

[6)] *Department of Physics and Astronomy, Williams College, Williamstown, Massachusetts 01267, USA*

[7)] *Leibniz-Institut für Kristallzüchtung, Max-Born-Str. 2, 12489 Berlin, Germany*

[8)] *Deparment of Physics, Pennsylvania State University, University Park, PA 168010, USA*

[9)] *Department of Materials Science and Engineering, Ohio State University, Columbus, OH 43210 USA*

[10)] *Department of Electrical and Computer Engineering, Ohio State University, Columbus, OH 43210 USA*

(Dated: 28 July 2026)

[a)] Authors contributed equally

[b)] ahadi.4@osu.edu

I. PHONON FREQUENCIES AND ENERGY GAINS FROM FIRST PRINCIPLES

The atomic structure relaxation, phonon, and Berry phase calculations were performed using first-principles density functional theory within the generalized gradient approximation (GGA) as implemented in the PBEsol functional[1] by the Vienna Ab initio Simulation Package (VASP)[2] with the ion-electron interaction described by the projector augmented wave method[3] including the spin-orbit coupling (SOC) effects. We employed an energy cutoff of 700 eV, Gaussian smearing of 0.005 eV, and electronic energy tolerance of 10^{-8} eV for the total energy convergence. The ionic relaxations were performed with a force tolerance of 10^{-3} Å/eV and an electronic momentum k-point mesh of $24 \times 24 \times 24$. Phonon and Berry phase calculations were performed with an electronic momentum k-point mesh of $16 \times 16 \times 16$. Phonon calculations were analyzed using the Phonopy code[4].

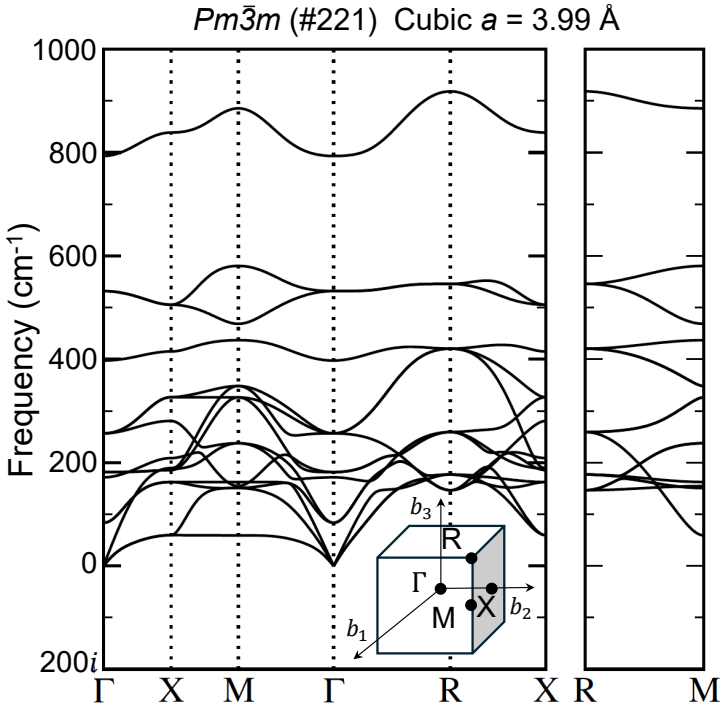


Fig. S1. Phonon band diagram for unstrained $KTaO_3$.

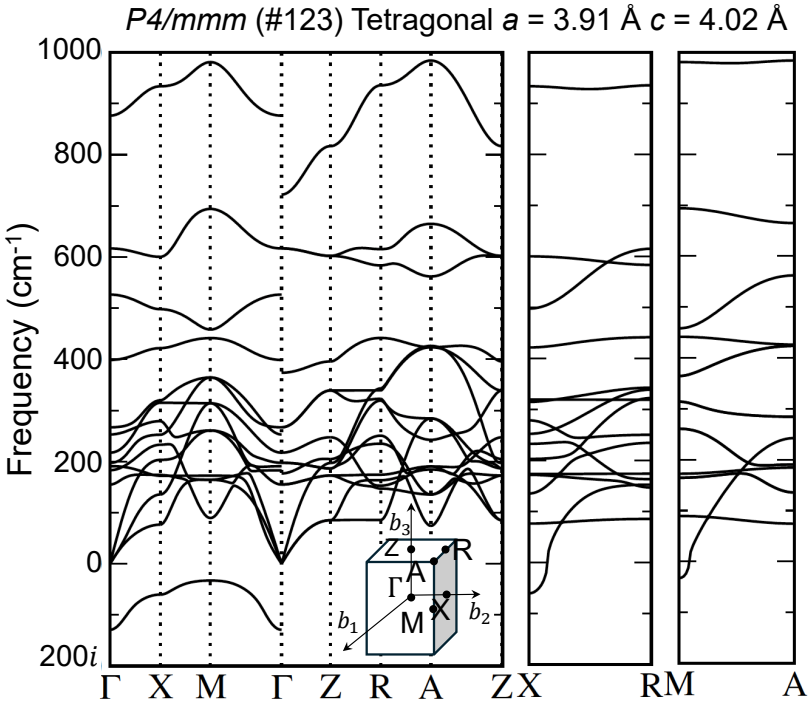


Fig. S2. Phonon band diagram for epitaxial strain conditions on $SrTiO_3$ (-2.1%).

II. DERIVATION OF PHASE FIELD MODEL AND FERROELECTRIC TRANSITION TEMPERATURE

Based on the Landau-Ginzburg-Devonshire theory of ferroelectrics, the Gibbs free energy density g can be written as a power series of the polarization near the phase transition.[5]

$$\begin{aligned} g = g(T, P_i, \sigma_i) - g(T, P_i) = 0, \sigma_i = 0 \\ = \alpha_1(T)(P_1^2 + P_2^2 + P_3^2) + \alpha_{11}(P_1^4 + P_2^4 + P_3^4) + \alpha_{12} \\ (P_1^2P_2^2 + P_1^2P_3^2 + P_2^2P_3^2) - \frac{1}{2}s_{11}(\sigma_1^2 + \sigma_2^2 + \sigma_3^2) - s_{12} \\ (\sigma_1\sigma_2 + \sigma_1\sigma_3 + \sigma_3\sigma_2) - \frac{1}{4}s_{44}(\sigma_4^2 + \sigma_5^2 + \sigma_6^2) - Q_{11} \\ (\sigma_1P_1^2 + \sigma_2P_2^2 + \sigma_3P_3^2) - Q_{12}(\sigma_1(P_2^2 + P_3^2) + \sigma_2(P_1^2 + P_3^2) + \\ \sigma_3(P_1^2 + P_2^2)) - Q_{44}(P_2P_3\sigma_4 + P_1P_3\sigma_5 + P_1P_2\sigma_6), \quad (1) \end{aligned}$$

where P_i represents the i^{th} component of polarization and σ_i represents the i^{th} component of the applied stress in Voigt notation. s_{11}, s_{11}, and s_{44} are the elastic compliance constants of

the cubic phase, and Q_{11}, Q_{12}, and Q_{44} are the electrostrictive coefficients. The rectangular Cartesian frame of reference is used the the x_1, x_2, and x_3 axes along the (100), (010), and (001) crystallographic directions. The Landau expansion coefficients α_1, α_{11}, and α_{12} along with the elastic compliance constants and the elctrostrictive coefficents for the potential function are listed in Table S1.

TABLE S1. Set of coefficients of the potential function

Coefficients	Values
T_O	1.6 K
T_S	18 K
C	6.98 $\times 10^4$ K
$\alpha_1(T)$	$\frac{1}{2\varepsilon_c C}\left(T_S \coth\left(\frac{T_S}{T}\right) - T_o\right)$ C^{-2} m^6 N
α_{11}	3 $\times 10^9$ C^{-4} m^6 N
α_{12}	3.3 $\times 10^9$ C^{-4} m^6 N
s_{11}	2.555 $\times 10^{-12}$ Pa^{-1}
s_{12}	-0.493 $\times 10^{-12}$ Pa^{-1}
s_{44}	9.174 $\times 10^{-12}$ Pa^{-1}
Q_{11}	0.0872 C^{-2} m^4
Q_{12}	-0.023 C^{-2} m^4
Q_{44}	0.0297 C^{-2} m^4

To investigate the effect of strain on the phase transitions of $KTaO_3$ thin films epitaxially grown on a substrate, we use the thin film boundary conditions and the modified free energy f for the strained thin film case.[6]

$$f = \alpha_1^*\left(P_1^2 + P_1^2\right) + \alpha_3^* P_3^2 + \alpha_{11}^*\left(P_1^4 + P_1^4\right) + \alpha_{33}^* P_3^4 + \alpha_{11}^*\left(P_1^2 P_3^2 + P_2^2 P_3^2\right) + \alpha_{12}^*\left(P_1^2 P_2^2\right) + \frac{\epsilon_s^2}{s_{11} + s_{12}} \tag{2}$$

with

$$\alpha_1^* = \alpha_1 - \frac{(Q_{11} + Q_{12})\,\epsilon_s}{s_{11} + s_{12}} \tag{3}$$

$$\alpha_3^* = \alpha_1 - \frac{2Q_{12}\epsilon_s}{s_{11} + s_{12}} \tag{4}$$

$$\alpha_3^* = \alpha_{11} - \frac{\left(Q_{11}^2 + Q_{12}^2\right) s_{11} - 2Q_{11}Q_{12}s_{11}}{2\left(s_{11}^2 - s_{12}^2\right)} \tag{5}$$

$$\alpha_{33}^* = \alpha_{11} + \frac{Q_{12}^2}{s_{11} + s_{12}} \tag{6}$$

$$\alpha_{12}^* = \alpha_{12} - \frac{1}{s_{11}^2 - s_{12}^2}\left[\left(Q_{11}^2 + Q_{12}^2\right) s_{12} - 2Q_{11}Q_{12}s_{11}\right] + \frac{Q_{44}^2}{2s_{44}} \tag{7}$$

$$\alpha_{13}^* = \alpha_{12} + \frac{Q_{12}\left(Q_{11} + Q_{12}\right)}{s_{11} + s_{12}} \tag{8}$$

where ϵ_s represents the misfit strain and in this case, $\epsilon_s = \frac{a_{sub} - a_o}{a_{sub}}$ where a_{sub} is the lattice constant of the substrate and a_o is the lattice constant of the unstrained cubic film.

The ferroelectic transition temperature can be calculated by solving the equation $T_c = \max(T_C^1, T_C^2)$ where T_C^1 and T_C^2 are solutions to

$$\alpha_1\left(T_C^1\right) + \Delta\alpha_1 = \alpha_1 T_C^1 - \frac{\left(Q_{11} + Q_{12}\right)\epsilon_s}{s_{11} + s_{12}} = 0 \tag{9}$$

and

$$\alpha_1\left(T_C^2\right) + \Delta\alpha_3 = \alpha_1 T_C^2 - \frac{2Q_{12}\epsilon_s}{s_{11} + s_{12}} = 0 \tag{10}$$

which allows us to construct the phase transition boundaries between the paraelectric and ferroelectric phases in the temperature-strain phase diagram marked by the dotted lines as illustrated in Fig. 1a. The dotted boundaries are calculated using the single set of coefficients (See Supplemental discussion and Table S2).

Since there is some variation in the data collected on the electrostrictive coefficients and elastic constants from the literature, we list the values by different groups in Table S2 and S3, and include the regions indicating the range of ferroelectric transition to account for the spread in these values.

TABLE S2. Electrostrictive coefficients in units of C^{-2} m^4

	Ref. 7	Ref 8
Q_{11}	0.087 ± 0.006	0.1256
Q_{12}	-0.023 ± 0.002	-0.0313
Q_{44}	0.0297 ± 0.023	-

TABLE S3. Elastic compliances in units of 10^{-12} Pa^{-1}

	Ref 9	Ref 10	Ref 10	Ref 11
s_{11}	2.555	2.47	2.17	2.36
s_{12}	-0.493	-0.325	-0.254	-0.307
s_{44}	9.174	5.9	5.076	11.69

III. ADDITIONAL SAMPLE CHARACTERIZATION OF $KTaO_3$ FILMS

High-resolution X-ray diffraction (XRD; Panalytical Emperyean) using Cu $K_{\alpha 1}$ radiation was performed on $KTaO_3$ thin films grown on different substrates. Figure S3 show θ-2θ scans of phase-pure epitaxial (001)-oriented $KTaO_3$ films on three different substrates ($SrTiO_3$, $DyScO_3$, and $GdScO_3$). In total 9.3 nm of $KTaO_3$ were deposited on $SrTiO_3$ (001) and 18 nm on each of $DyScO_3$ $(110)_o$ and $GdScO_3$ $(110)_o$. The presence of Laue fringes indicate that each film has a well-defined thickness i.e., smooth interfaces between film and substrate and between film and air. These Laue fringes around the thin films peak were used to calculate the thickness and were equal to the thickness extracted from HAADF-STEM. The in-plane lattices constants of the strained $KTaO_3$ films shown in Fig. 2d were determined from the 00ℓ (ℓ=1,2,3) reflection peaks. Supplementary Figure S5a shows the reciprocal space

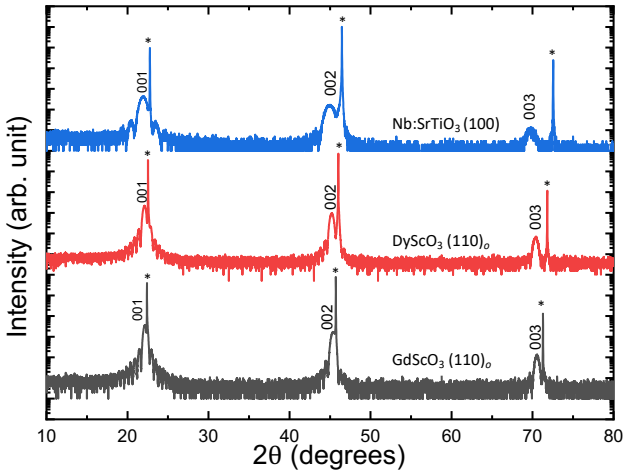


Fig. S3. θ-2θ XRD scan of $KTaO_3$ films on (001) $SrTiO_3$ (blue), $(110)_o$ $DyScO_3$, (red) and $(110)_o$ $GdScO_3$ (grey) substrates.

maps (RSM) around the 103 $KTaO_3$ and 332 $DyScO_3$ $(110)_o$. The film is commensurately

strained to the substrate. The FWHM of the rocking curves of film (0.009°/0.003°) and substrate (0.008°/0.003°) are comparable, suggesting high crystalline quality (Supplementary Fig. S5b,d). The rocking curves were measured along the [001] and [1$\bar{1}$0] in-plane directions of the $DyScO_3$ substrate, respectively. This is the narrowest FWHM ever reported for a $KTaO_3$ film. Figure S5c,f shows AFM images at different magnifications. The root-mean-square (rms) roughness is 0.8 nm taking a 5 µm^2 area as the reference.

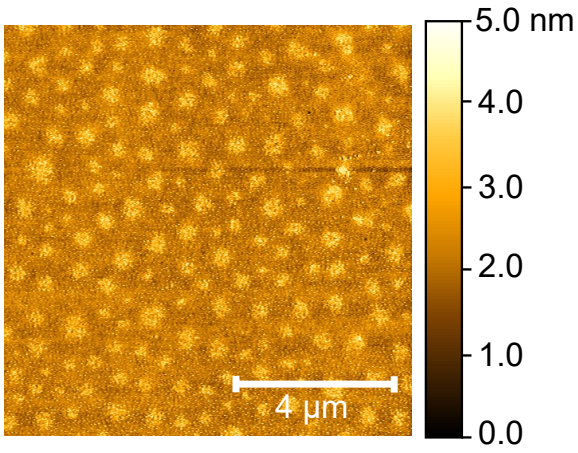


Fig. S4. AFM images of the untreated 9.3 nm thick $KTaO_3$ film shown through Figs. 2-4. This film exhibits an rms roughness of 0.8 nm over the whole 5 µm^2 scan.

Figure S6**a** shows the RSM around the 103 $KTaO_3$ and 332 $GdScO_3$ reflection and suggests that the film is commensurately strained to the substrate. The FWHM of the rocking curves of film (0.009°/0.008°) and substrate (0.017°/0.016°) comparable suggesting high crystalline quality (Fig. S5b,d). Figure S6 shows the AFM images at different magnifications with a rms of 0.6 nm taking a 5 µm^2 area as the reference.

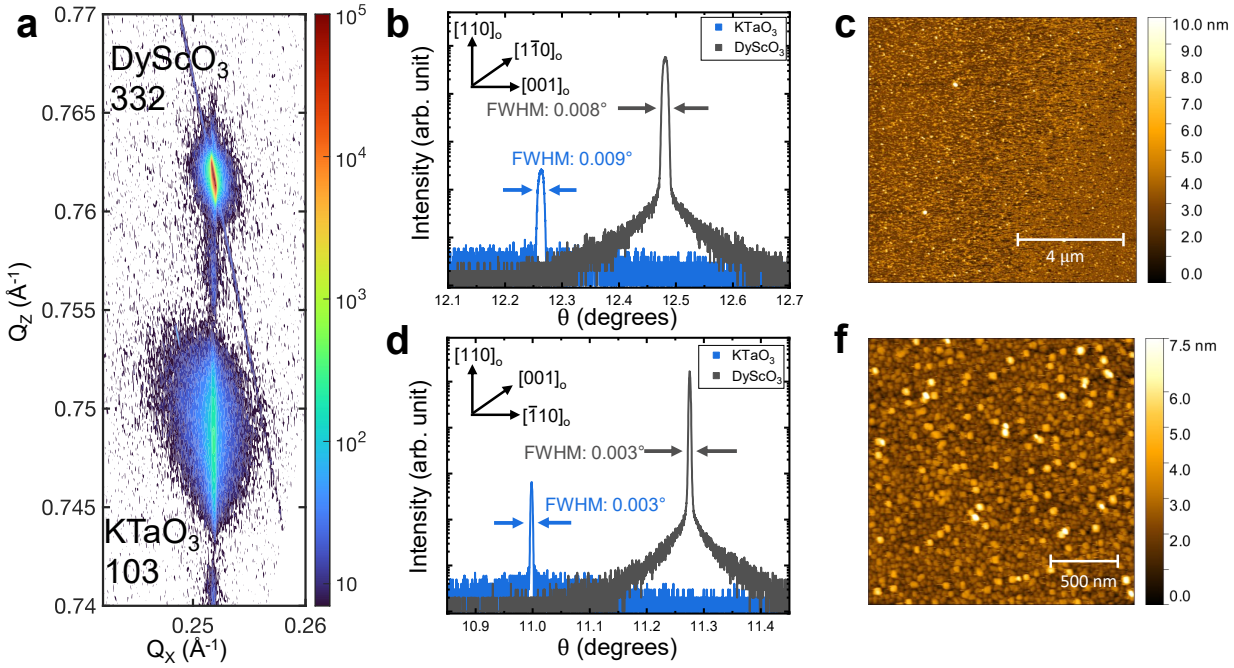


Fig. S5. **18 nm $KTaO_3$ on $DyScO_3$.** **a** RSM of the $KTaO_3$ 103 and $DyScO_3$ 332 peaks. **b and d** Overlaid rocking curves of the $KTaO_3$ 001 and $GdScO_3$ 110 peaks, showing comparable FWHMs, indicating low out-of-plance mosaicity ($\Delta\omega \approx 0.009°$ and $0.003°$ along the two orthogonal in-plane directions of the substrate.) **c,f** AFM images at different magnifications. The root mean square (rms) roughness over the $5\,\mu m^2$ scan is 0.9 nm.

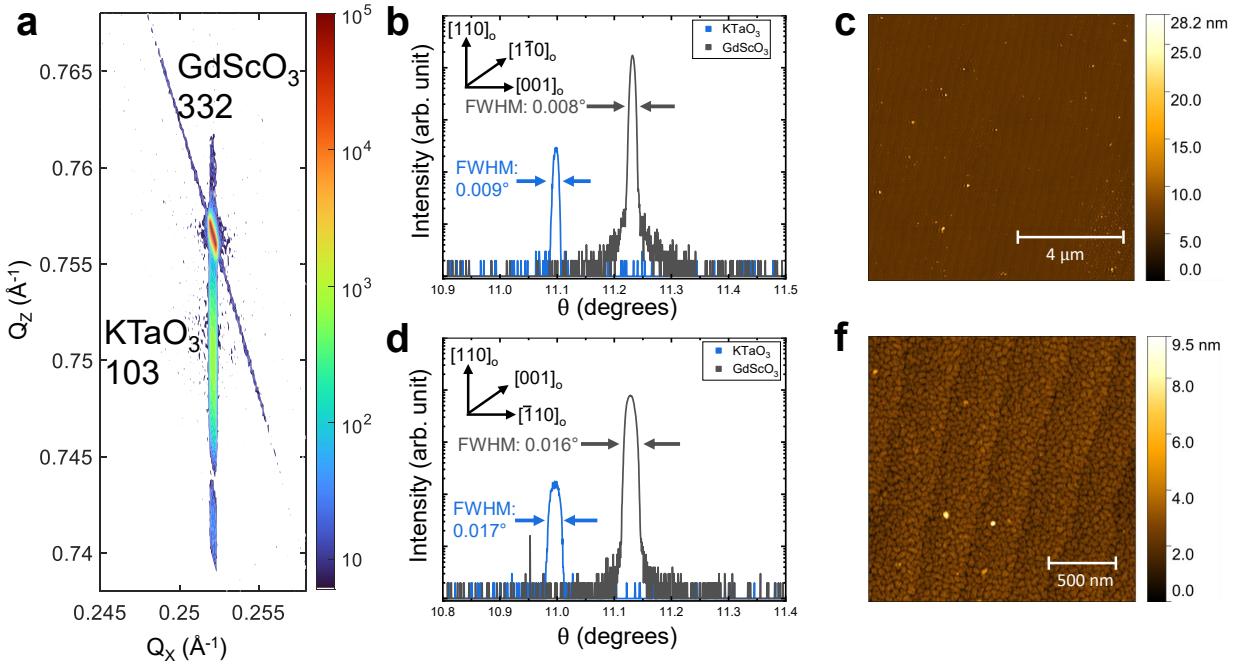


Fig. S6. **18 nm $KTaO_3$ on $GdScO_3$ a** RSM of the $KTaO_3$ 103 and $GdScO_3$ 332 peaks. **b and d** Overlaid rocking curves of the $KTaO_3$ 001 and $GdScO_3$ 110 peaks, showing comparable FWHMs, indicating low out-of-plance mosaicity ($\Delta\omega \approx 0.009°$ and $0.017°$ along the two orthogonal in-plane directions of the substrate.) **c,f** AFM images at different magnifications. The root mean square (rms) roughness over the $5\,\mu m^2$ scan is 0.6 nm.

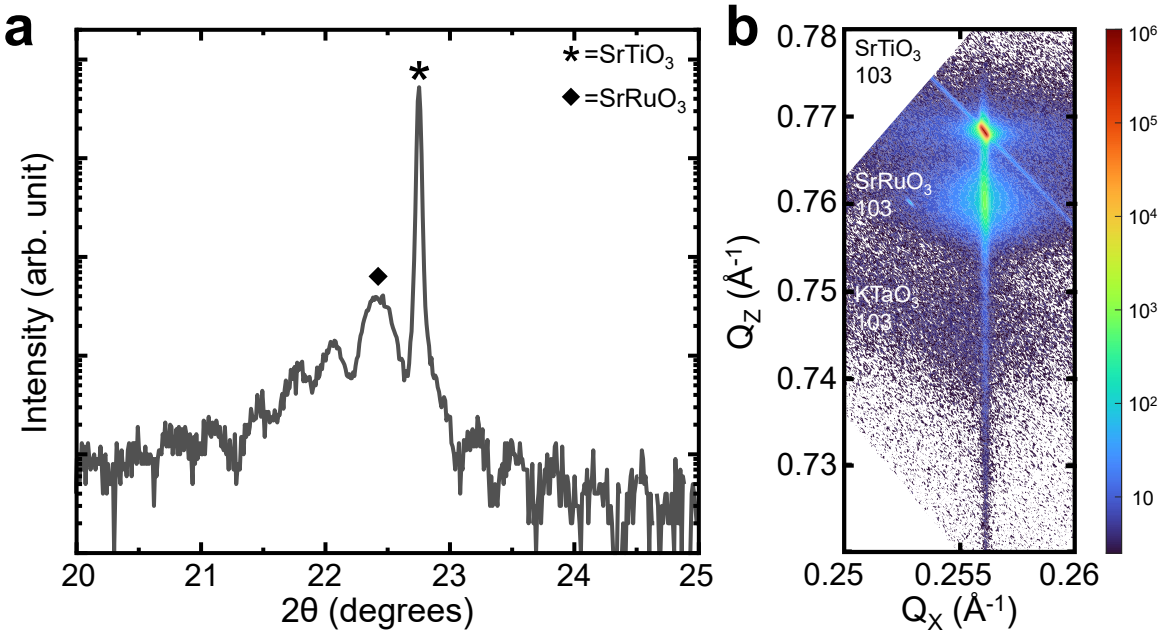


Fig. S7. **a** θ-2θ XRD scan of $KTaO_3$ films on a 35 nm thick bottom electrode $SrRuO_3$ deposited on a $SrTiO_3$ substrate. **b** RSM of the $KTaO_3$ 103, $SrRuO_3$ 332, and $SrTiO_3$ 103 peaks.

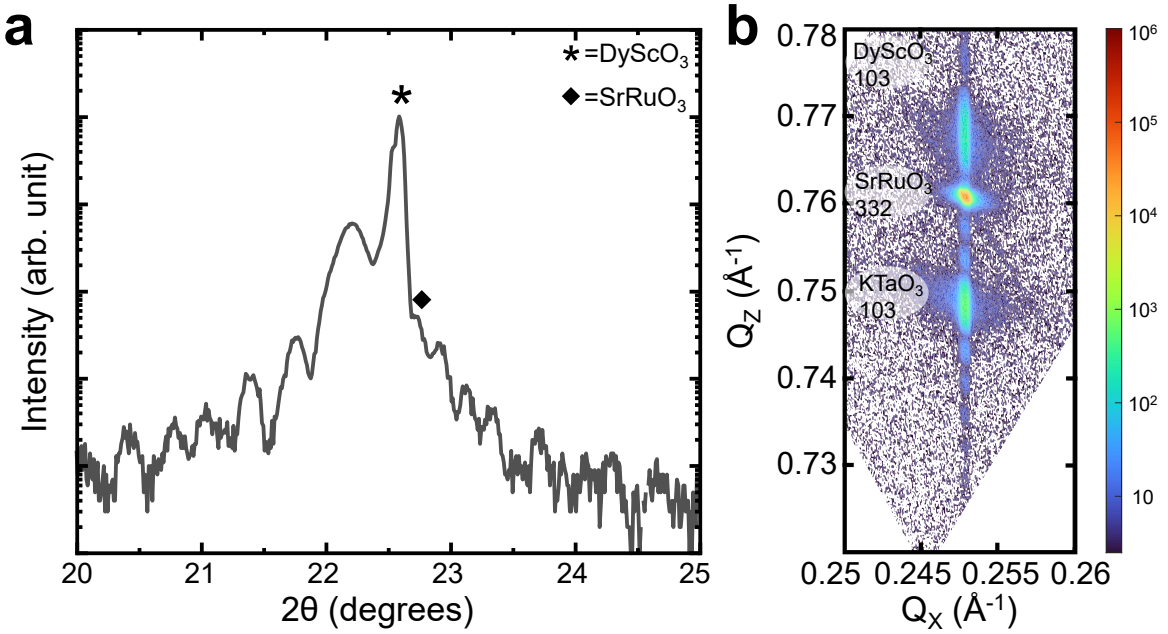


Fig. S8. **a** θ-2θ XRD scan of $KTaO_3$ films on a 20 nm thick bottom electrode $SrRuO_3$ deposited on a $DyScO_3$ substrate. **b** RSM of the $KTaO_3$ 103, $SrRuO_3$ 332, and $DyScO_3$ 332 peaks.

IV. THERMODYNAMIC ANALYSIS OF EFFECT OF STRAIN ON PARA AND FERROELECTRIC GROUND STATE OF $KTAO_3$

For a ferroelectric thin film epitaxially grown on a substrate, we may assume that the in-plane strains are fixed by the lattice parameter of the substrate and the out-of-plane components of stress are free to relax. Therefore, the in-plane components of strain (ε_1 , ε_2), and ε_6) and the out-of-plane components of stress (σ_3 , σ_4, and σ_5) will be independent variables leaving, the in-plane components of stress (σ_1 , σ_2, and σ_6) and the out-of-plane components of strain (ε_3, ε_4, and ε_5) as dependent variables. While equation S1 describes the thermodynamic behavior using stress as the independent variable and strain as the dependent variable, we can transform this equation to be more suitable for ferroelectric thin films,

$$f(T, P, \varepsilon_1, \varepsilon_2, \sigma_3) = u - Ts - \sigma_3\varepsilon_3 = g + \sigma_1\varepsilon_1 + \sigma_2\varepsilon_2 + \sigma_6\varepsilon_6 \tag{11}$$

To perform the Legendre transform, we must find $\sigma_1(T, P, \varepsilon_1, \varepsilon_2, \sigma_3)$, $\sigma_2(T, P, \varepsilon_1, \varepsilon_2, \sigma_3)$ and $\sigma_6(T, P, \varepsilon_1, \varepsilon_2, \sigma_3)$. For simplicity we shall only consider the impact of normal strains. To do this we shall first calculate

$$\varepsilon_1(T, P, \sigma_1, \sigma_2, \sigma_3) = -\left(\frac{\partial g}{\partial \sigma_1}\right)_{T,P} = Q_{11}P_1^2 + Q_{12}(P_2^2 + P_3^2) + S_{11}\sigma_1 + S_{12}(\sigma_2 + \sigma_3) \tag{12}$$

$$\varepsilon_2(T, P, \sigma_1, \sigma_2, \sigma_3) = -\left(\frac{\partial g}{\partial \sigma_2}\right)_{T,P} = Q_{11}P_2^2 + Q_{12}(P_1^2 + P_3^2) + S_{11}\sigma_2 + S_{12}(\sigma_1 + \sigma_3) \tag{13}$$

Then algebraically solve for $\sigma_1(T, P, \varepsilon_1, \varepsilon_2, \sigma_3)$ and $\sigma_2(T, P, \varepsilon_1, \varepsilon_2, \sigma_3)$ which yields

$$\sigma_1 = \frac{\varepsilon_1 - (Q_{11}P_1^2 + Q_{12}(P_2^2 + P_3^2)) - (S_{12} - \frac{S_{12}^2}{S_{11}})\sigma_3 + \frac{S_{12}}{S_{11}}(Q_{11}P_2^2 + Q_{12}(P_2^2 + P_3^2) - \varepsilon_2)}{S_{11} - \frac{S_{12}^2}{S_{11}}}, \tag{14}$$

$$\sigma_2 = \frac{\varepsilon_2 - (Q_{11}P_2^2 + Q_{12}(P_1^2 + P_3^2)) - (S_{12} - \frac{S_{12}^2}{S_{11}})\sigma_3 + \frac{S_{12}}{S_{11}}(Q_{11}P_1^2 + Q_{12}(P_1^2 + P_3^2) - \varepsilon_1)}{S_{11} - \frac{S_{12}^2}{S_{11}}}. \tag{15}$$

Substituting in these expressions for $\sigma_1(T, P, \varepsilon_1, \varepsilon_2, \sigma_3)$ and $\sigma_2(T, P, \varepsilon_1, \varepsilon_2, \sigma_3)$ in equation 2.1 we obtain an expression that uses the in-plane strain and the out-of-plane stress as the independent variables.

$$f(T,P,\varepsilon_1,\varepsilon_2,\sigma_3) =$$
$$g(T,P,\sigma_1(T,P,\varepsilon_1,\varepsilon_2,\sigma_3),\sigma_1(T,P,\varepsilon_1,\varepsilon_2,\sigma_3),\sigma_3)+\sigma_1(T,P,\varepsilon_1,\varepsilon_2,\sigma_3)\varepsilon_1+\sigma_2(T,P,\varepsilon_1,\varepsilon_2,\sigma_3)\varepsilon_2 \tag{16}$$

Where the out-of plane strain is found by taking the derivative of the free-energy with respect to the out-of plane stress

$$\varepsilon_3 = \left(\frac{\partial f}{\partial \sigma_3}\right)_{T,P,\varepsilon_1,\varepsilon_2} \tag{17}$$

Assuming we have a tetragonal C domain $P_i = (0, 0, P_3)$, we can find that the out-of plane strain is

$$\varepsilon_3 = \frac{(\varepsilon_1+\varepsilon_2)S_{12}}{S_{11}+S_{12}} + \left(Q_{11} - \frac{2Q_{12}S_{12}}{S_{11}+S_{12}}\right)P_3^2 \tag{18}$$

Then, to obtain the lattice parameter one can use the relation

$$\varepsilon_3 = \frac{c - a^{eq}}{a^{eq}}, \tag{19}$$

where $a^{eq}$is the equivalent cubic lattice parameter of a stress-free, polarization-free, cubic $KTaO_3$. Combining equation 20 and 21 we find,

$$c = a^{eq}[1 + \frac{(\varepsilon_1+\varepsilon_2)S_{12}}{S_{11}+S_{12}} + (Q_{11} - \frac{2Q_{12}S_{12}}{S_{11}+S_{12}})P_3^2], \tag{20}$$

In the paraelectric phase, $P_i = (0, 0, 0)$, which yields

$$c = a^{eq}[1 + \frac{(\varepsilon_1+\varepsilon_2)S_{12}}{S_{11}+S_{12}}], \tag{21}$$

and reduces to the solution derived from elasticity theory.

V. STATISTICAL ANALYSIS OF ATOMIC DISPLACEMENTS

The displacement distributions shown in Figs. S9-S12 were compiled from multiple HAADF-STEM images acquired from several analyzed regions of each sample. For each region, the positions of the K columns and the four neighboring Ta columns were obtained by 2D Gaussian fitting, and the displacement of the K column relative to the centroid of the surrounding Ta columns was extracted. The resulting pooled distributions are used to

compare the net polar distortions in $KTaO_3$ films grown on different substrates. For $KTaO_3$ grown on $DyScO_3$, the pooled displacement distribution compiled from multiple HAADF-STEM images and analyzed regions shows a slight net out-of-plane bias. The extracted mean values are $\langle d_x \rangle$= -1.6 pm and $\langle d_z \rangle$= 4.6 pm, indicating a weak preferential displacement along the out-of-plane [001] direction. This result is consistent with a weak out-of-plane polar distortion in the DyScO3-strained film at room temperature, smaller than that observed for the $SrTiO_3$-strained case. To further clarify the $DyScO_3$ case, we also analyzed a cross-sectional lamella prepared from the same $DyScO_3$-based capacitor heterostructure for which ferroelectric switching is shown in Fig. S14. In this switched device region, the extracted displacement distribution yields $\langle d_x \rangle$= -4.3 pm and $\langle d_z \rangle$= 21.2 pm, with the principal axis oriented primarily along the out-of-plane direction and an aspect ratio of 1.59. This reveals a clear net out-of-plane polar distortion in the active device region. The larger out-of-plane displacement compared with the pooled $DyScO_3$ film data is consistent with spatial heterogeneity of the polar distortion and with the weaker, near-transition character of the $DyScO_3$-strained film. In contrast, for $KTaO_3$ grown coherently on $GdScO_3$, the pooled displacement distribution does not show a net out-of-plane polar distortion. The extracted mean values are $d_x = -12.3$ pm and $d_z = -1.2$ pm, indicating that the average out-of-plane displacement remains centered near $d_z \approx 0$. Here, the finite in-plane mean displacement is not negligible. However, we do not interpret it as evidence for the strain-induced out-of-plane tetragonal polar state discussed in the main text. This distinction is based on the direction of the displacement and its consistency with complementary measurements. The measured mean displacement in $KTaO_3/GdScO_3$ is primarily in-plane, whereas the polar state discussed in the main text is out-of-plane and tetragonal. In addition, the $GdScO_3$ film shows no SHG signal beyond the bare substrate down to 4 K, no extended out-of-plane lattice constant, and no ferroelectric switching. We use "correlated polar distortion" to refer to a spatially coherent displacement pattern that produces a net symmetry breaking detectable by complementary probes such as SHG, XRD, or switching measurements. By this definition, the $GdScO_3$ film does not show a long-range correlated out-of-plane polar state. The finite pooled $\langle d_x \rangle$ is instead consistent with possible local structural heterogeneity and short-range distortions in this weakly strained film, rather than with a coherent net out-of-plane polar state. Figure S12 shows the pooled two-dimensional displacement distribution for $KTaO_3$ grown on $SrTiO_3$. The distribution exhibits a strong net out-of-plane bias,

with $\langle d_x \rangle$= -3.1 pm and $\langle d_z \rangle$= 46.3 pm. Unlike the $DyScO_3$ and $GdScO_3$ cases, the STO distribution is not unimodal, but instead exhibits two dominant populations with opposite in-plane displacements and similar positive out-of-plane components. This indicates that while the average in-plane displacement remains near zero, the out-of-plane polar distortion is robust and common to both local populations. The bimodal distribution therefore reflects locally distinct in-plane offsets superimposed on the same predominantly out-of-plane polar state, rather than a reversal of the out-of-plane polarization. A quantitative summary of the principal-axis-based analysis of the pooled displacement distribution is given in Table S4. Here, $\langle d_x \rangle$ and $\langle d_z \rangle$ describe the average in-plane and out-of-plane displacements, respectively. The principal-axis angle θ gives the overall orientation of the pooled distribution, while σ_{major} and σ_{minor} describe its characteristic widths along the major and minor axes. Their ratio provides a compact measure of the overall elongation of the pooled cloud. Because the STO distribution is bimodal, these quantities should be interpreted only as a summary of the overall shape of the distribution; the contour plot more directly captures the existence of the two local populations. The positive $\langle d_z \rangle$ confirms a strong average out-of-plane polar displacement, while the near-zero $\langle d_x \rangle$ indicates that the opposite in-plane components largely cancel on average. The aspect ratio of 1.30 indicates moderate elongation of the pooled distribution. Together, these parameters provide a compact summary of the overall distribution, while the contour plot in Fig. S12 more clearly reveals the physically important two-lobed structure.

TABLE S4. Quantitative summary of the pooled 2D displacement distribution for $KTaO_3$ grown on $SrTiO_3$.

Parameter	**Meaning**	**Value**
$\langle d_x \rangle$ = (pm)	Mean in-plane displacement	-3.1
$\langle d_z \rangle$ = (pm)	Mean out-of-plane displacement	46.3
θ (deg)	Orientation of the principal axis of the distribution	154.5
σ_{major} (pm)	Standard deviation along the major principal axis	27.1
σ_{minor} (pm)	Standard deviation along the minor principal axis	20.8
σ_{major} /σ_{minor}	Aspect ratio of the distribution	1.30

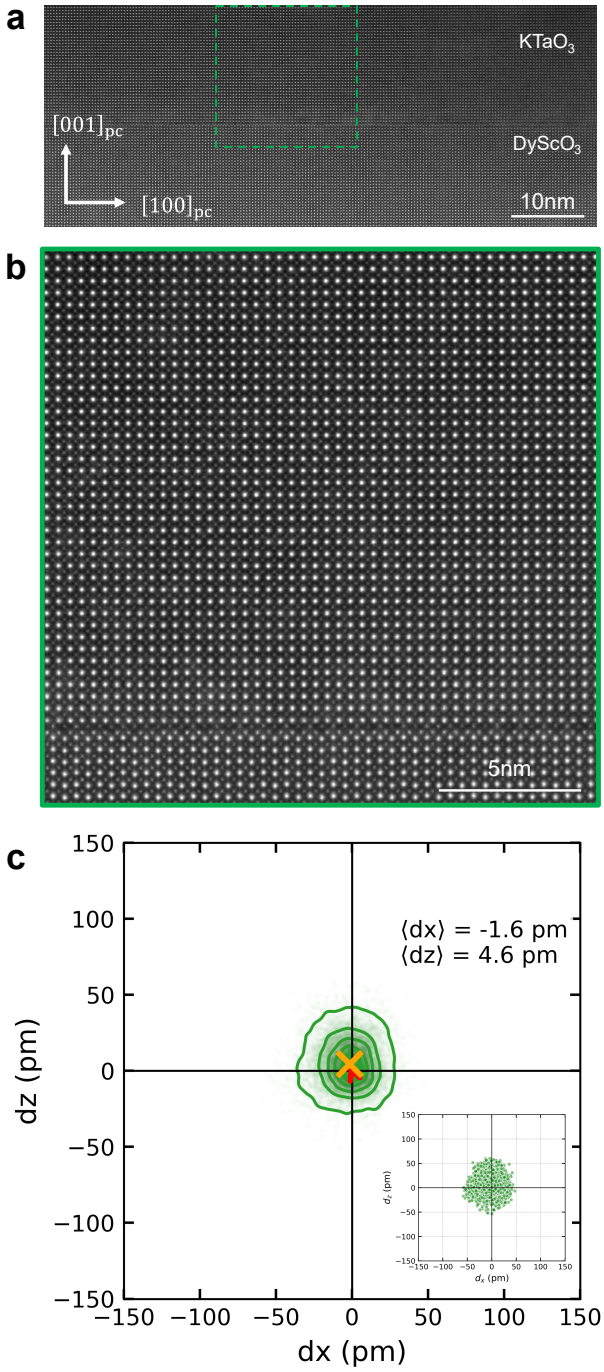


Fig. S9. **a,b** HAADF-STEM images of the $KTaO_3/DyScO_3$ heterostructure. **c** Pooled two-dimensional distribution of K-column displacements relative to the centroid of the four neighboring Ta columns, compiled from multiple HAADF-STEM images acquired from several analyzed regions. The contour lines summarize the distribution, and the orange marker denotes the mean displacement.

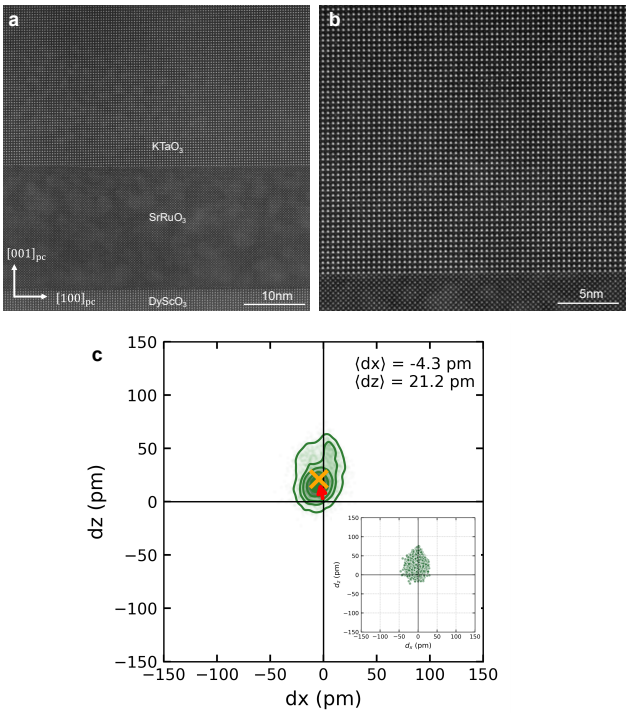


Fig. S10. Statistical analysis of atomic displacements in the $DyScO_3$-based capacitor heterostructure measured to exhibit ferroelectric switching. **a,b** HAADF-STEM images of the $KTaO_3/SrRuO_3/DyScO_3$ heterostructure from the same device for which switching is shown in Fig. S14. **c** Pooled two-dimensional distribution of atomic displacements in the analyzed region of the switched device. The contour lines summarize the distribution, and the orange marker denotes the mean displacement.

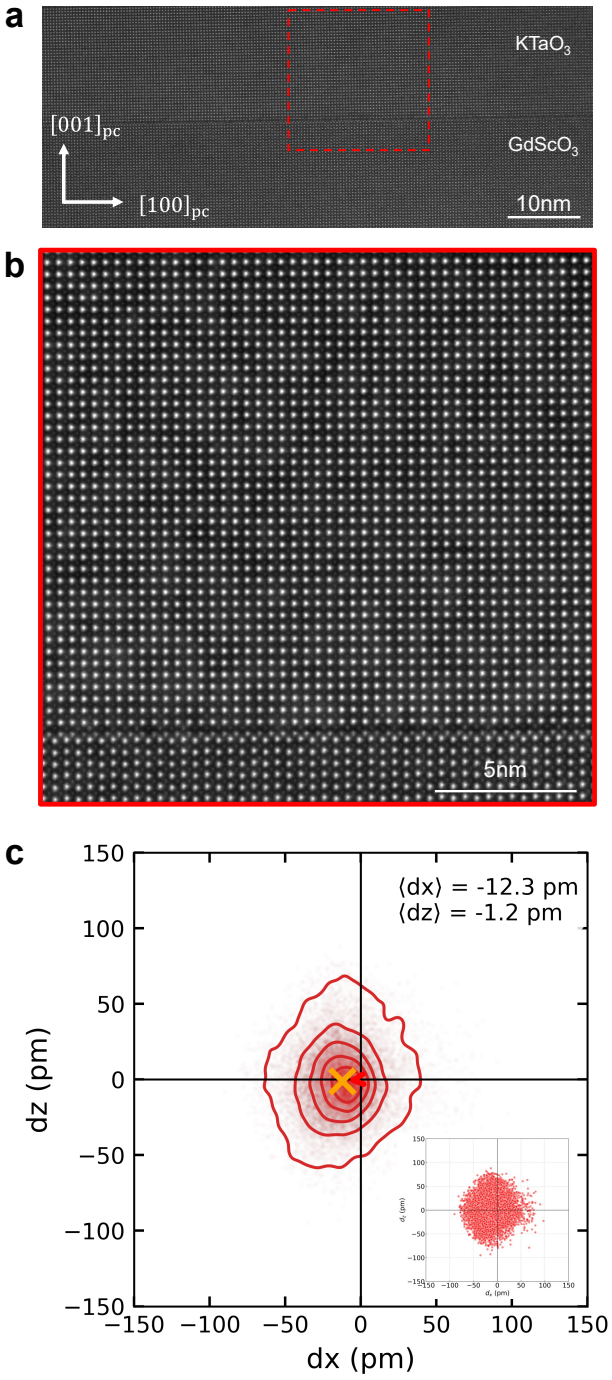


Fig. S11. Statistical analysis of atomic displacements in $KTaO_3$ grown on $GdScO_3$. **a,b** HAADF-STEM images of the $KTaO_3/GdScO_3$ heterostructure. **c** Pooled two-dimensional distribution of K-column displacements in the analyzed regions. The contour lines summarize the distribution, and the orange marker denotes the mean displacement.

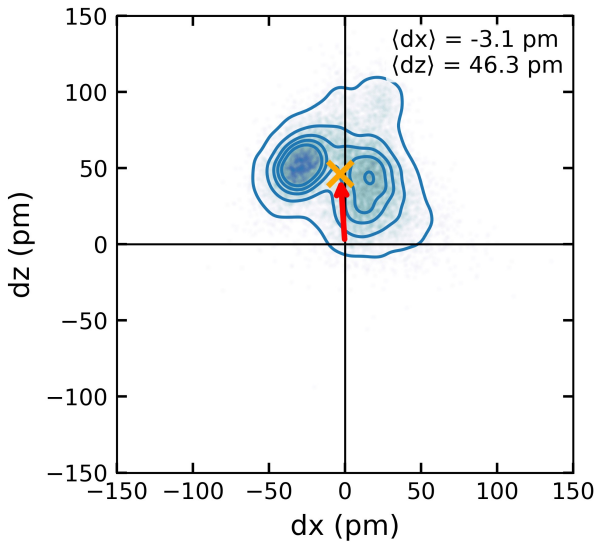


Fig. S12. Statistical analysis of atomic displacements in $KTaO_3$ grown on $SrTiO_3$. Pooled two-dimensional displacement distribution compiled from multiple HAADF-STEM images acquired from several analyzed regions. The contour plot shows two dominant populations with opposite in-plane displacements and similar positive out-of-plane components. The orange marker denotes the mean displacement.

VI. BORN EFFECTIVE CHARGES FROM FIRST PRINCIPLES

Born effective charges were calculated from the linear response within the VASP package. The Born effective charge Z^* matrices for each strain are shown in Table S5.

TABLE S5. Born effective charge Z^* matrices in $|e|$ for each element with different strain.

element	$KTaO_3$ (bulk)	$GdScO_3$ (-0.5 %)	$DyScO_3$ (-0.9 %)	$SrTiO_3$ (-2.1 %)
K	$\begin{pmatrix} 1.21 & 0.00 & 0.00 \\ 0.00 & 1.21 & -0.03 \\ 0.00 & 0.00 & 1.21 \end{pmatrix}$	$\begin{pmatrix} 1.27 & 0.00 & 0.00 \\ 0.00 & 1.19 & 0.00 \\ 0.00 & 0.04 & 1.19 \end{pmatrix}$	$\begin{pmatrix} 1.23 & 0.00 & 0.00 \\ 0.00 & 1.19 & 0.02 \\ 0.00 & 0.03 & 1.20 \end{pmatrix}$	$\begin{pmatrix} 1.25 & 0.00 & 0.00 \\ 0.00 & 1.22 & 0.01 \\ 0.00 & 0.01 & 1.21 \end{pmatrix}$
Ta	$\begin{pmatrix} 5.06 & 0.00 & 0.00 \\ 0.00 & 4.32 & 0.23 \\ 0.00 & -0.23 & 4.32 \end{pmatrix}$	$\begin{pmatrix} 4.99 & 0.00 & 0.00 \\ 0.00 & 8.22 & 0.04 \\ 0.00 & -0.13 & 8.03 \end{pmatrix}$	$\begin{pmatrix} 4.85 & 0.00 & 0.00 \\ 0.00 & 7.99 & 0.03 \\ 0.00 & -0.14 & 7.44 \end{pmatrix}$	$\begin{pmatrix} 4.65 & 0.00 & 0.00 \\ 0.00 & 7.66 & 0.11 \\ 0.00 & -0.06 & 6.59 \end{pmatrix}$
O	$\begin{pmatrix} -1.25 & 0.00 & 0.00 \\ 0.00 & -3.51 & -0.07 \\ 0.00 & -0.16 & -0.99 \end{pmatrix}$	$\begin{pmatrix} -1.21 & 0.00 & 0.00 \\ 0.00 & -6.40 & -0.11 \\ 0.00 & -0.31 & -1.52 \end{pmatrix}$	$\begin{pmatrix} -1.09 & 0.00 & 0.00 \\ 0.00 & -6.10 & -0.05 \\ 0.00 & -0.15 & -1.50 \end{pmatrix}$	$\begin{pmatrix} -1.06 & 0.00 & 0.00 \\ 0.00 & -5.93 & -0.03 \\ 0.00 & -0.06 & -1.40 \end{pmatrix}$
O	$\begin{pmatrix} -3.77 & 0.00 & 0.00 \\ 0.00 & -1.03 & -0.30 \\ 0.00 & 0.30 & -1.03 \end{pmatrix}$	$\begin{pmatrix} -3.83 & 0.00 & 0.00 \\ 0.00 & -1.46 & -0.01 \\ 0.00 & 0.15 & -1.59 \end{pmatrix}$	$\begin{pmatrix} -3.82 & 0.00 & 0.00 \\ 0.00 & -1.60 & -0.02 \\ 0.00 & 0.09 & -1.52 \end{pmatrix}$	$\begin{pmatrix} -3.70 & 0.00 & 0.00 \\ 0.00 & -1.53 & -0.01 \\ 0.00 & 0.07 & -1.41 \end{pmatrix}$
O	$\begin{pmatrix} -1.25 & 0.00 & 0.00 \\ 0.00 & -0.99 & 0.16 \\ 0.00 & 0.07 & -3.51 \end{pmatrix}$	$\begin{pmatrix} -1.22 & 0.00 & 0.00 \\ 0.00 & -1.55 & 0.16 \\ 0.00 & 0.25 & -6.11 \end{pmatrix}$	$\begin{pmatrix} -1.18 & 0.00 & 0.00 \\ 0.00 & -1.48 & 0.02 \\ 0.00 & 0.18 & -5.62 \end{pmatrix}$	$\begin{pmatrix} -1.14 & 0.00 & 0.00 \\ 0.00 & -1.42 & -0.08 \\ 0.00 & 0.03 & -4.98 \end{pmatrix}$

VII. DERIVATION OF OPTICAL SECOND HARMONIC GENERATION (SHG) POLARIMETRY EXPRESSION FOR THE TETRAGONAL PHASE *4mm*

Symmetry analysis of the $KTaO_3$ thin films was performed through fitting SHG polarimetry to analytical model as described below. The orientation of the substrate with respect to lab coordinates (x_1, x_2, x_3) are described in Fig. 4a. All measurements are done in reflection geometry.

The induced nonlinear polarization, $P^{2\omega}$,and the incident electric field, E^{ω}, is related in a second harmonic generation process as,

$$P_i^{2\omega} \propto d_{ijk} E_j^{\omega} E_k^{\omega} \tag{22}$$

where, the proportionality constants depend on the incident beam fluence, beam shape, and Fresnel coefficients at the film-air, film-substrate interfaces and thickness of the films[12]. d_{ijk} is the nonlinear susceptibility tensor and depends on the symmetry of the material in the crystal physics. For tetragonal $4mm$ point group symmetry, d_{ijk} has the following form in Voigt notation:

$$d_{ij} = \begin{pmatrix} 0 & 0 & 0 & 0 & d_{15} & 0 \\ 0 & 0 & 0 & d_{15} & 0 & 0 \\ d_{31} & d_{31} & d_{33} & 0 & 0 & 0 \end{pmatrix} \tag{23}$$

The linearly polarized incident electric field E^{ω} is rotated by φ and hence has the form $E_{\omega} = (E_{\omega}\cos(\psi), E_{\omega}\sin(\psi), 0)$. Taking into account the oblique incidence measurement geometry, the electric field in the crystal axes coordinates can be written as $(E_0\cos(\varphi)\cos(\theta), E_0\sin(\varphi), -E_0\cos(\varphi)\sin(\theta))$, where θ is the angle of incidence.

The induced polarization in the crystal physics coordinates, $i = (1, 2, 3)$, can be calculated through equation 3, which can be rotated back to (x_1, x_2, x_3) coordinates to give the p and s-polarized components of SHG ($p||X$ and $s||Y$). The p and s-polarized SHG intensities can be expressed as follows:

$$\begin{gathered} I_p^{2\omega} \propto \left(P_p^{2\omega}\right)^2 \propto \left((2d_{15} - d_{31} - d_{33})\cos[\varphi]^2 - 2d_{31}\sin[\varphi]^2\right)^2 \\ I_s^{2\omega} \propto \left(P_s^{2\omega}\right)^2 \propto d_{15}^2 \sin[2\varphi]^2 \end{gathered} \tag{24}$$

VIII. INCIDENT POWER DEPENDENCE SHG MEASUREMENTS

Figure S11 shows the SHG intensity as a function of incident laser power measured for strained and relaxed $KTaO_3$ films on $SrTiO_3$, $DyScO_3$, and $GdScO_3$ substrates. While strained films on $SrTiO_3$ and $DyScO_3$ substrates show SHG beyond bare substrate, the relaxed films and the films grown on $GdScO_3$ do not show SHG signal beyond their respective bare substrates.

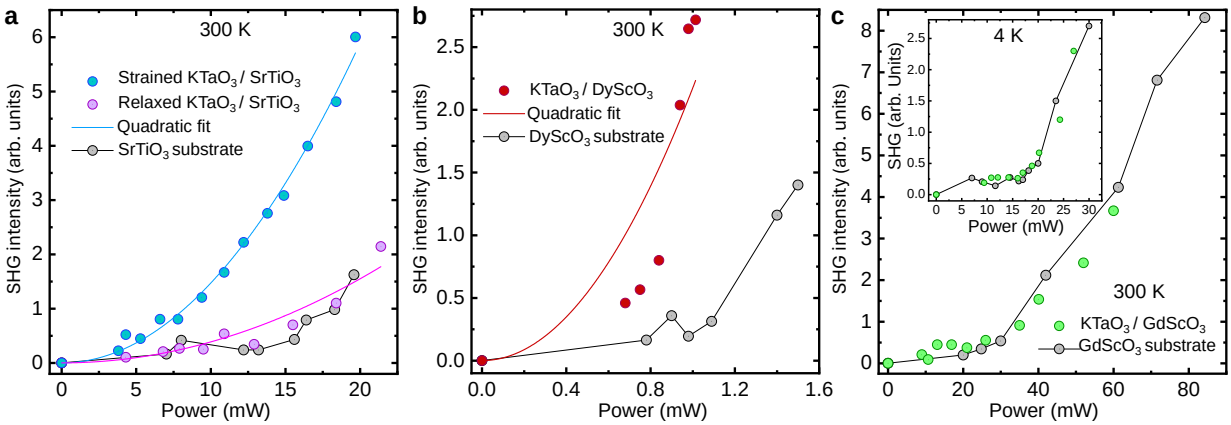


Fig. S13. **a**. SHG intensity as a function of incident laser power measured for strained and relaxed $KTaO_3$ films on $SrTiO_3$ substrate compared to similar measurement on a bare $SrTiO_3$ substrate. Thinner strained $KTaO_3$ film (9 nm thick) shows a prominent SHG response quadratically scaling with the incident fundamental laser power. Thicker relaxes $KTaO_3$ film (19 nm thick), however, shows no SHG response relative to the bare $SrTiO_3$ substrate. **b** Quadratically scaling power depedent SHG response of strained $KTaO_3$ films grown on $DyScO_3$ substrate. **c** Power dependent SHG measured on strained $KTaO_3$ film grown on $GdScO_3$ shows no SHG response different from measurements on bare $GdScO_3$ substrate.

IX. PIEZO FORCE MICROSCOPY OF $KTaO_3$ ON $DyScO_3$

Figure SS14 shows the $KTaO_3/SrRuO_3/DyScO_3$ capacitor hetero-structure is investigated using PFM. A 180° phase reversal for the out-of-plane PFM response is observed. The structural characterization details of this sample are discussed in Supplemental Discussion III.

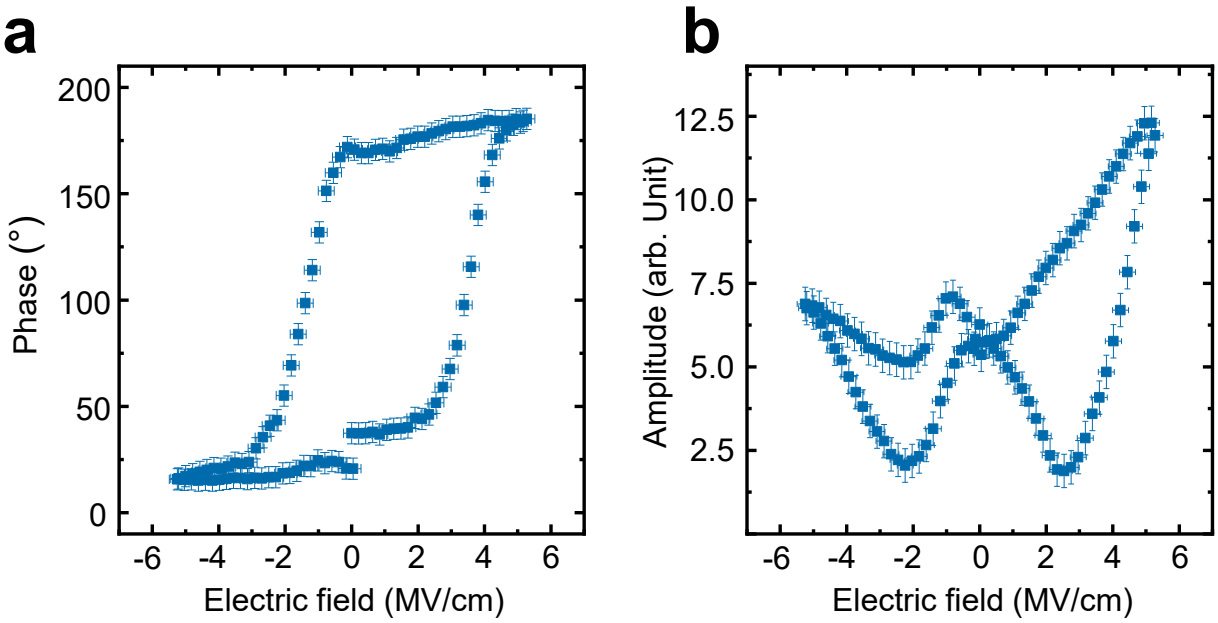


Fig. S14. **a** PFM switching using the $KTaO_3/SrRuO_3/DyScO_3$ sample showing a upward build-in field. **b** Magnitude of piezo response.

REFERENCES

[1]J. P. Perdew, A. Ruzsinszky, G. I. Csonka, O. A. Vydrov, G. E. Scuseria, L. A. Constantin, X. Zhou, and K. Burke, "Restoring the Density-Gradient Expansion for Exchange in Solids and Surfaces," Phys. Rev. Lett. **100**, 136406 (2008).

[2]G. Kresse and J. Furthmüller, "Efficient iterative schemes for ab initio total-energy calculations using a plane-wave basis set," Phys. Rev. B **54**, 11169–11186 (1996).

[3]G. Kresse and D. Joubert, "From ultrasoft pseudopotentials to the projector augmented-wave method," Phys. Rev. B **59**, 1758–1775 (1999).

[4]A. Togo, L. Chaput, T. Tadano, and I. Tanaka, "Implementation strategies in phonopy and phono3py," J. Phys. Condens. Matter **35**, 353001 (2023).

[5]M. J. Haun, E. Furman, S. Jang, H. McKinstry, and L. Cross, "Thermodynamic theory of $PbTiO_3$," Journal of Applied Physics **62**, 3331–3338 (1987).

[6]N. Pertsev, A. Zembilgotov, and A. Tagantsev, "Effect of mechanical boundary conditions on phase diagrams of epitaxial ferroelectric thin films," Physical review letters **80**, 1988 (1998).

[7]H. Uwe and T. Sakudo, "Electrostriction and stress-induced ferroelectricity in $KTaO_3$," Journal of the Physical Society of Japan **38**, 183–189 (1975).

[8]D. S. Tanner, P.-E. Janolin, and E. Bousquet, "Strain-engineered divergent electrostriction in $KTaO_3$," Physical Review B **106**, L060102 (2022).

[9]J. W. Fleming, M. J. Weber, G. W. Day, A. Feldman, B. H. Chai, M. G. Kuzyk, W. R. Holland, C. F. Rapp, M. Minden, D. T. Moore, *et al.*, *Handbook of optical materials* (CRC press, 2018).

[10]H. Bouafia, S. Hiadsi, B. Abidri, A. Akriche, L. Ghalouci, and B. Sahli, "Structural, elastic, electronic and thermodynamic properties of $KTaO_3$ and $NaTaO_3$: Ab initio investigations," Computational materials science **75**, 1–8 (2013).

[11]S. Cabuk, "Ab initio volume-dependent elastic and lattice dynamics properties of $KTaO_3$," physica status solidi (b) **247**, 93–97 (2010).

[12]R. Zu, B. Wang, J. He, J.-J. Wang, L. Weber, L.-Q. Chen, and V. Gopalan, "Analytical and numerical modeling of optical second harmonic generation in anisotropic crystals using shaarp package," npj Computational Materials **8**, 246 (2022).